OUKA
The University of Osaka
Institutional Knowledge Archive

Title	Studies on Fluoride Ion Conducting Solids Based on Rare-Earth Oxyfluoride
Author(s)	百相, 瑞貴
Citation	大阪大学, 2024, 博士論文
Version Type	VoR
URL	https://doi.org/10.18910/96041
rights	
Note	

The University of Osaka Institutional Knowledge Archive : OUKA

https://ir.library.osaka-u.ac.jp/

The University of Osaka

Doctoral Dissertation

Studies on Fluoride Ion Conducting Solids Based on Rare-Earth Oxyfluoride

(希土類オキシフッ化物を母体とするフッ化物イオン伝導性固体に関する研究)

Mizuki Momai

January 2024

Division of Applied Chemistry
Graduate School of Engineering
Osaka University

Preface

The study in this thesis has been conducted under direct supervision of Professor Dr. Nobuhito Imanaka at the Division of Applied Chemistry, Graduate School of Engineering, Osaka University.

The objective of this thesis is to investigate the crystal structural and fluoride ion conducting properties of rare-earth oxyfluorides.

The author hopes that the results and insights obtained in this research contribute to the further development of novel solid electrolyte and that the materials would be utilized for practical applications.

Mizuki Momai

Division of Applied Chemistry
Graduate School of Engineering,
Osaka University,
2-1 Yamadaoka, Suita,
Osaka 565-0871,
JAPAN

January 2024

Contents

General Introduction 1

Chapter 1

The Effect of Anion Defects on the Crystal Phase and Fluoride Ion Conductivity in Lanthanum Oxyfluoride

1.1 Introduction 4

1.2 Experimental Procedure 4

1.3 Results and Discussions 5

1.4 Conclusion 11

Chapter 2

Improvement of Fluoride Ion Conductivity by Strict Control of Lattice Volume and Fluoride Ion Concentration in Lanthanum Oxyfluoride

2.1 Introduction 12

2.2 Experimental Procedure 12

2.3 Results and Discussions 13

2.4 Conclusion 22

Chapter 3

Crystal Phase and Fluoride Ion Conducting Behavior of Nonstoichiometric Rare-earth Oxyfluorides.

3.1 Introduction 23

3.2 Experimental Procedure 23

3.3 Results and Discussions 24

3.4 Conclusion 33

Summary 34

References 36

Lists of Publications 38

Acknowledgements 39

General Introduction

Electrical conduction in solids is occurred by the macroscopic migration of electronic (electron: e^- or hole: h^+) or ion species, and the materials whose charge carriers are electronic species are known as metals or semiconductors. On the other hand, there are unique solids whose charge carriers are ions having non-negligible volume, unlike the electronic species, and they are called “solid electrolytes”. In general, solid electrolyte has a characteristic that only single ion species can migrate in the solid because multi-ion conduction in the solid means a destruction of the lattice. Because of such unique character of selective ion migration, solid electrolytes are considered as key materials for various electrochemical devices such as all-solid-state batteries [1, 2], fuel cells [3, 4], and chemical sensors [5, 6].

In the field of solid electrolytes, ion conducting nature is greatly influenced by the ion size and valence state of mobile ion. Relatively large ions are fundamentally difficult to conduct in rigid crystal structures because sufficient space is required for ionic migration in a material. In addition, ions with high valence bond to surrounding counter ions through strong electrostatic interactions, making them more difficult to move than ions with low valence. Based on these fundamental constraints in physical chemistry, highly conductive ions in solids are limited to monovalent cations (e.g. Li^+, Na^+ or H^+ ion [7-9]) and divalent cations (e.g. Mg^{2+} or Ca^{2+} ion [10, 11]) with relatively small ionic size, and there are many reports on the migration of these ions in solids. In contrast, for the anions whose ionic size are generally larger than cations are difficult to migration in solids, but fluoride ion (F^-) has been known to show exceptionally high ionic conductivity due to its relatively small ionic size and low valence state. Therefore, some F^- ion conducting solids are applied to the fluoride ion-selective electrodes [12]. In these days, the developments of the F^- ion conductors with high ionic conductivity are intensively conducted for application to all-solid-state fluoride-ion batteries (FIBs), which are expected to show higher energy density than lithium-ion batteries [13-16].

In the various types of fluorine-containing materials, simple metal fluorides such as $PbSnF_4$ [17],

BaF_2 [18, 19], and LaF_3 [20, 21] have been studied as candidates for fluoride ion conductors with high conductivities. Among them, $PbSnF_4$ solid has been considered as the leading candidate for the electrolyte material of FIBs because of extraordinal high F^- conductivity at room temperature (1.5×10^{-3} $S \cdot cm^{-1}$) [17]. However, $PbSnF_4$ solid cannot be used as a constituent material of FIBs due to its low stability under reducing conditions. Therefore, it is highly demanded to develop the novel fluoride ion conductors with high chemical stability as well as high F^- conductivity.

In this study, I focused on the rare-earth oxyfluorides (*R*OFs; *R* = rare-earth element) as the mother solid of novel fluoride ion conductor because *R*OFs have been reported to have higher chemical stability in atmospheric air compared with the corresponding rare-earth fluorides (RF_3) owing to containing O^{2-} ions in the lattice [22-24]. The *R*OFs have been reported to possess various kind of crystal structures depending on rare-earth element, like tetragonal (space group: *P*4/*nmm*) and trigonal (space group: $R\bar{3}m$) phases for LaOF [25-27] and orthorhombic (space group: *Abm*2) phase in addition to trigonal $R\bar{3}m$ phase for GdOF [28]. Moreover, the phase transition between *P*4/*nmm* and $R\bar{3}m$ phases of LaOF with conductivity change has been reported [26, 27], but the mechanism of the phase transition is still unclear. In addition, there are few reports on ion conduction properties of other *R*OFs solids except for the LaOF solid. Therefore, in order to use *R*OF solids as the practical materials, the following points must be satisfied:

- To clarify the factor that decides the crystal structure of *R*OF solids
- To investigate the ion conducting property in each crystal phase of *R*OF
- To improve the F^- ion conductivity of the *R*OF solids

The main purpose of this thesis is to develop a novel fluoride ion conducting solids based on *R*OF through the deep understanding of the structural and ion conducting properties for the *R*OF solids. For this purpose, I synthesized various kinds nonstoichiometric compositional *R*OFs ($RO_{1-y}F_{1+2y}$ and $La_{1-x}M_xO_{1-\delta}F$ (M: divalent cations)) by intentionally varying F/O ratio and/or by replacing R^{3+} ion

site with divalent cations to investigate the phase transition nature of *R*OF, together with stoichiometrical *R*OF.

This thesis consists of the following three chapters.

In Chapter 1, I selected LaOF, which has been reported as a F^- conductor, as the target material, and improved the F^- ion conductivity with suppression of the phase transition of LaOF solid by doping Mg^{2+} ions into the lanthanum oxyfluoride to form the $La_{1-x}Mg_xO_{1-\delta}F$ ($0 \leq x \leq 0.3$) solids with O^{2-} ion defects.

In Chapter 2, I synthesized nonstoichiometric lanthanum oxyfluorides, $LaO_{1-y}F_{1+2y}$, with intentionally varying F/O ratio to investigate both the phase transition behavior and the fluoride ion conducting property of the LaOF solid in detail. Moreover, the $La_{1-x}Sr_xO_{0.6-0.5x-y}F_{1.8+2x}$ ($0 \leq x \leq 0.4$, $0 \leq y \leq 0.2$) solids were developed to introduce further F^- ions into the LaOF lattice for obtaining the solid with higher ionic conductivity than $LaO_{0.6}F_{1.8}$ solid.

In Chapter 3, nonstoichiometric rare-earth oxyfluorides, $RO_{1-y}F_{1+2y}$ ($0 \leq y \leq 0.4$; *R* = La, Pr, Nd, Sm, Eu, Gd, Tb, Dy, Ho, Er, Tm, and Yb), were systematically synthesized in order to investigate the relationship between the crystal phase and the ionic conductivity for the *R*OF solids. Furthermore, the local structure of the stoichiometric *R*OFs were investigated to clarify the reason for forming the different crystal phases depended on the rare-earth element and F/O ratio in the nonstoichiometric $RO_{1-y}F_{1+2y}$ solids.

Chapter 1

The Effect of Anion Defects on the Crystal Phase and Fluoride Ion Conductivity in Lanthanum Oxyfluoride

1.1 Introduction

Although only lanthanum oxyfluoride (LaOF) has been investigated the electrical conducting properties among the rare-earth oxyfluoride, its conductivity was too low to apply for the all-solid-state fluoride-ion batteries (FIBs). Furthermore, its conducting species have not been identified. In addition, LaOF shows the phase transition with varying electrical conductivity, and therefore, there remains many unclarified properties for LaOF.

In this chapter, I aim to improve the F^- ion conductivity of the LaOF solid by suppressing the phase transition. Here, I synthesized the $La_{1-x}Mg_xO_{1-\delta}F$ ($0 \leq x \leq 0.3$) solids in which the La^{3+} ion (ionic size: 0.130 nm, coordination number (CN) = 8 [29]) site in the LaOF solid was partially replaced by a smaller Mg^{2+} ion (0.103 nm (CN = 8) [29]). By doping Mg^{2+} ion into La^{3+} site in the LaOF lattice, O^{2-} ion defects which is expected as an ionic conduction pathway are generated as well as a lattice volume decrease. Moreover, contraction of the LaOF lattice may suppress the displacement of the constituent elements in the lattice, thereby suppressing phase transition.

1.2 Experimental Procedure

$La_{1-x}Mg_xO_{1-\delta}F$ ($0 \leq x \leq 0.3$) solids were synthesized by a solid-state reaction method. A stoichiometric amount of La_2O_3, LaF_3, and $Mg(NO_3)_2 \cdot 6H_2O$ were mixed by an agate motor and calcined at 800℃ for 12 h in synthetic air. After pelletizing the obtained powder, the sample pellet was sintered at the same condition. The synthesized samples were identified by X-ray powder diffraction (XRD; SmartLab, Rigaku) with Cu-Kα radiation (40 kV, 40 mA) by a step scanning method in the 2θ range between 10° to 70° with a step width of 0.04°. The lattice volume of the samples was estimated

from the XRD peak angles refined with α-Al_2O_3 as an internal standard material. To confirm the phase transition of the sample, the thermogravimetric and differential thermal analysis (TG-DTA; DTG-60AH, Shimadzu) was performed at heating and cooling rate of 10°C min^{-1}. The electrical conductivity of samples with Pt sputter thin films deposited on both surfaces was measured in the frequency range of 1 Hz to 13 MHz by the complex impedance method (1260 Impedance/Gain-Phase Analyzer, Solartron) at temperatures between 300 and 800°C in atmospheric air. In order to identify the conducting ion species, the modified Tubandt electrolysis was carried out by applying a DC Voltage of 5.0 V for the $La_{0.8}Mg_{0.2}O_{1-\delta}F$ sintered pellet at 600°C for 12 h in atmospheric air.

1.3 Results and Discussions

Figure 1.1 shows the XRD patterns of the $La_{1-x}Mg_xO_{1-\delta}F$ ($0 \leq x \leq 0.3$) solids after calcination at 800°C for 12 h in synthetic air. While the samples with $x \leq 0.2$ were obtained as the single-phase sample with tetragonal LaOF structure, the samples with $x \geq 0.25$ were the mixture of LaOF (tetragonal structure) and MgO. Figure 1.2 depicts the compositional dependence of the lattice volume of the tetragonal LaOF structure for the $La_{1-x}Mg_xO_{1-\delta}F$ solids. In the sample with $x \leq 0.2$, the lattice volume decreased with increasing Mg^{2+} ion content (x), suggesting that Mg^{2+} ions (0.103 nm (CN = 8) [29]) whose ionic size is smaller than La^{3+} ions (0.130 nm (CN = 8) [29]) partial replaced the La^{3+} ion site in the tetragonal LaOF structure, according to the following reaction [Eq. (1-1)].

$$\frac{1}{3}LaF_3 + \frac{2-3x}{6}La_2O_3 + xMg(NO_3)_2 \rightarrow La_{1-x}Mg_xO_{1-\delta}F + 2xNO_2 + \frac{1}{2}xO_2 \qquad (1\text{-}1)$$

On the other hand, the lattice volume of the tetragonal LaOF structure in the samples with $x \geq 0.25$ were larger than that of mother solid of LaOF, despite smaller Mg^{2+} ions were doped into La^{3+} site. Although the $La_{1-x}Mg_xO_{1-\delta}F$ solids with no F^- ion vacancy was prepared by mixing La_2O_3, LaF_3, and $Mg(NO_3)_2 \cdot 6H_2O$, the solids with high concentration Mg^{2+} ion cannot hold the single-phase of tetragonal LaOF structure due to the large lattice contraction. As a result, MgO was formed as the secondary phase for the samples with $x > 0.2$, while the excess amount of F^- ion may be inserted into

the interstitial sites of the tetragonal LaOF structure [Eq. (1-2)].

$$\frac{1}{3}LaF_3+\frac{2\text{-}3x}{6}La_2O_3+xMg(NO_3)_2 \rightarrow \frac{5\text{-}5x}{4}La_{0.8}Mg_{0.2}O_{1\text{-}\delta}F_{1+n}+\frac{5x\text{-}1}{4}MgO+2xNO_2+xO_2 \quad (1\text{-}2)$$

Here, n = (5x−1)/(5−5x), which is the excess amount of F^- ion. The lattice for samples with $x \geq 0.25$ expands monotonically with x as excess F^- ions are inserted into the LaOF lattice. From XRD result, it was considered that the solid solubility limit composition of the $La_{1-x}Mg_xO_{1-\delta}F$ solid was $x = 0.2$.

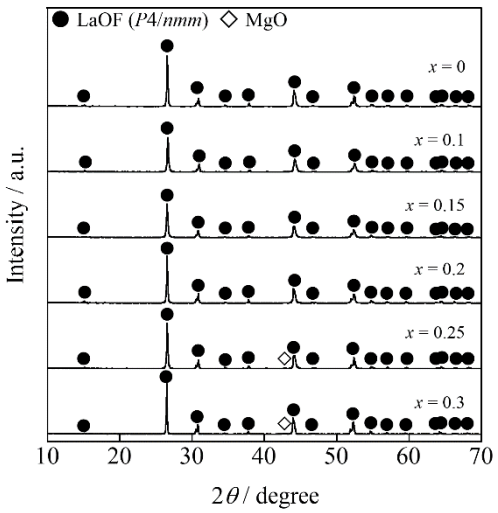


Figure 1.1 XRD patterns of the $La_{1-x}Mg_xO_{1-\delta}F$ ($0 \leq x \leq 0.3$) solids.

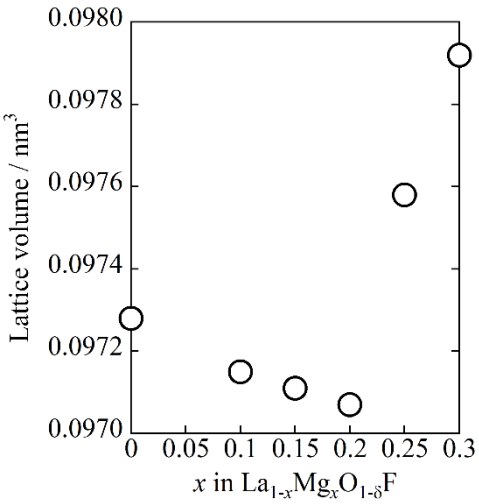


Figure 1.2 Lattice volume of the $La_{1-x}Mg_xO_{1-\delta}F$ ($0 \leq x \leq 0.3$) solids.

In order to investigate the phase transition behavior of LaOF, the thermogravimetry and differential thermal analysis (TG-DTA) was performed for the $La_{1-x}Mg_xO_{1-\delta}F$ solids obtained as the single-phase samples ($x \leq 0.2$). Figure 1.3 shows the TG-DTA results for the solids with $x \leq 0.2$. The samples with $x \leq 0.1$ showed clear endothermic and exothermic DTA peaks around 500°C with no meaningful weight change during heating and cooling processes, respectively. In addition, the peak intensities became weaker with increasing Mg^{2+} ion content (x). In contrast, such DTA peaks were not observed for the samples with $x \geq 0.15$. This behavior implies that the phase transition may appear for the $La_{1-x}Mg_xO_{1-\delta}F$ ($x \leq 0.1$) solids. To reveal the phase transition behavior, in-situ XRD measurements were performed for the $La_{1-x}Mg_xO_{1-\delta}F$ ($x = 0, 0.2$) solids. Figure 1.4 displays the XRD patterns for the $La_{1-x}Mg_xO_{1-\delta}F$ ($x = 0, 0.2$) solids between 300 and 800°C in cooling step. While the LaOF ($x = 0$) solid

possessed tetragonal ($P4/nmm$) LaOF structure above 600°C and trigonal ($R\bar{3}m$) LaOF structure below 500°C (Figure 1.4(a)), $La_{0.8}Mg_{0.2}O_{0.9}F$ (x = 0.2) solid possessed tetragonal LaOF structure at all temperatures (Figure 1.4(b)). The results indicate that LaOF (x = 0) solid exhibits a tetragonal to trigonal phase transition at around 500°C, and that this phase transition is gradually suppressed by doping Mg^{2+} ions into the LaOF solid. This is because the shrinkage of LaOF lattice suppress the displacement of the ion in the lattice. However, although it was clarified that the LaOF (x = 0) solid possessed trigonal LaOF structure below 500°C, the sintered sample possessed tetragonal LaOF structure at room temperature (shown Figure 1.1). To reveal the reason why the trigonal structure was observed at lower temperatures for the LaOF (x = 0) solid by this experiment, XRD measurement at 400°C was performed for the LaOF (x = 0) solid with tetragonal structure at room temperature. Figure 1.5 shows change over time of the XRD pattern of LaOF (x = 0) held at 400°C. A gradual change from tetragonal to trigonal structure was observed, and such structural change completed after 1 h. This result strongly indicates that the displacement of the ion in the LaOF which causes phase transition needs time, especially below 500°C.

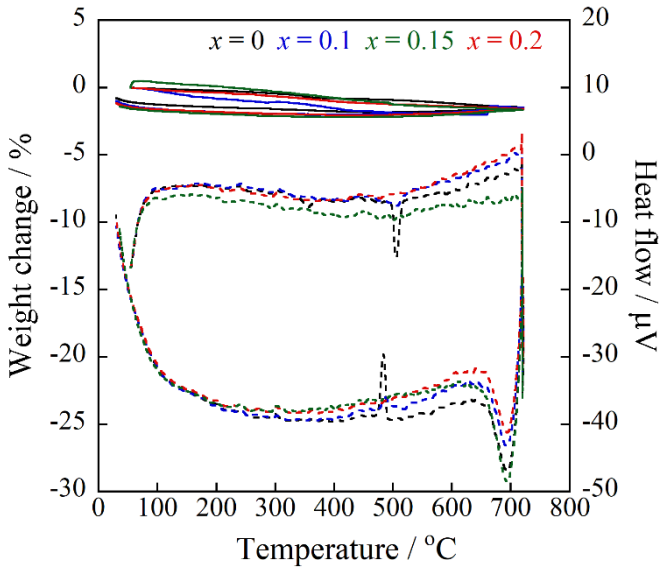


Figure 1.3 TG (solid line) and DTA (dotted line) curves for the $La_{1-x}Mg_xO_{1-\delta}F$ ($0 \leq x \leq 0.2$) solids.

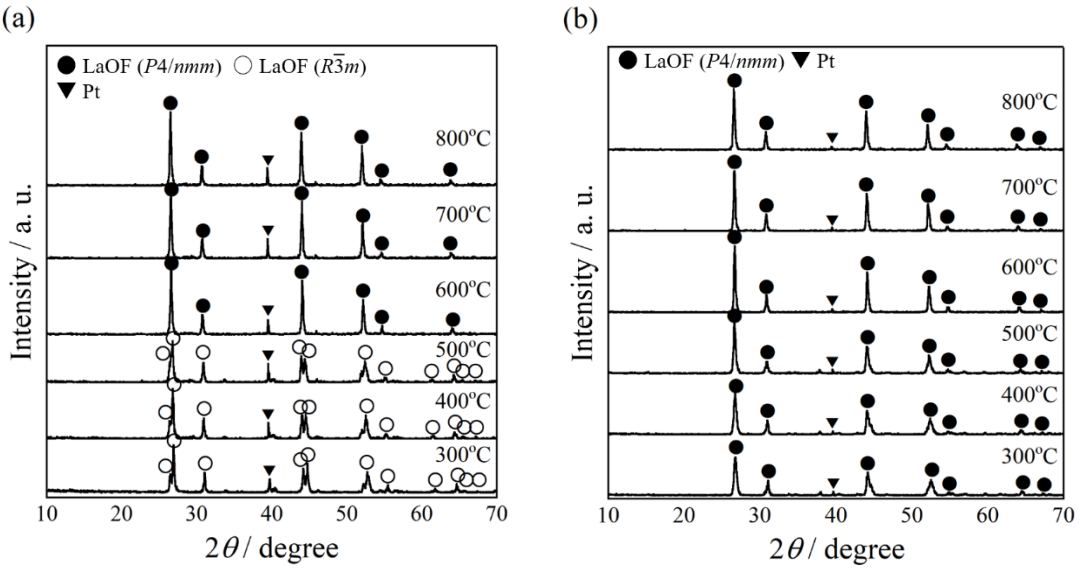


Figure 1.4 In-situ XRD patterns of the (a) LaOF (x = 0) and (b) $La_{0.8}Mg_{0.2}O_{1-\delta}F$ (x = 0.2) solids between 300 and 800 °C in cooling step.

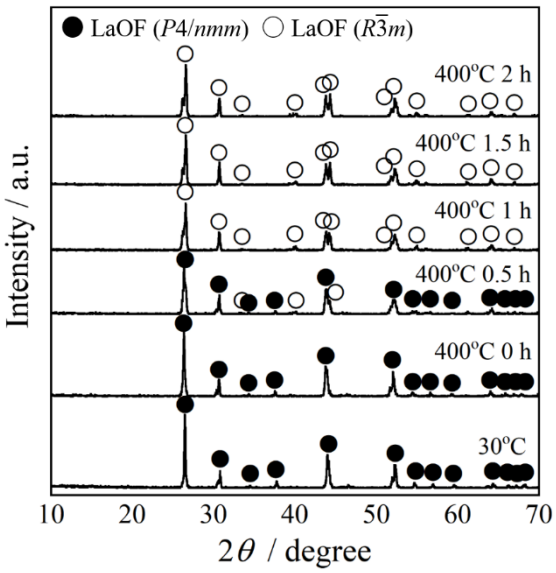


Figure 1.5 XRD patterns of the LaOF solid maintained at 400°C.

Figure 1.6 depicts the temperature dependence of the ac conductivity for the $La_{1-x}Mg_xO_{1-\delta}F$ solids with the corresponding data for LaOF possessed tetragonal and trigonal structure reported in the literature [27]. For the samples showing the phase transition ($x \leq 0.1$), the conductivity gradient changes were clearly observed between 500 and 600°C, and each gradient in the higher or lower temperature region is in good agreement with the reported value for tetragonal or trigonal LaOF solid,

respectively. On the other hand, the conductivities for the samples with $x \geq 0.15$ linearly changed from 300 to 800°C. These results indicate that the phase transition of the $La_{1-x}Mg_xO_{1-\delta}F$ ($x \leq 0.1$) solids observed between 500 and 600°C accompanies a conductivity change. Among the samples obtained as the single-phase of tetragonal structure, the $La_{0.8}Mg_{0.2}O_{1-\delta}F$ ($x = 0.2$) solid with the solid solubility limit composition showed the highest conductivity of 6.9×10^{-3} S·cm^{-1} which is ca. 46.5 times higher than that of LaOF ($x = 0$) solid at 800°C.

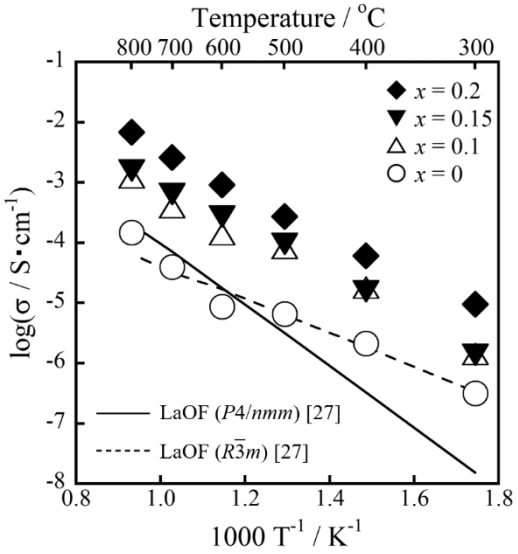


Figure 1.6 Temperature dependence of the ionic conductivity for the $La_{1-x}Mg_xO_{1-\delta}F$ ($0 \leq x \leq 0.2$) solids with the corresponding data for the reported tetragonal and trigonal LaOF solids [27].

In order to identify the conducting ion species in the $La_{0.8}Mg_{0.2}O_{1-\delta}F$ ($x = 0.2$) solid exhibiting the highest conductivity among the prepared samples, modified Tubandt electrolysis using three sample pellets (three $La_{0.8}Mg_{0.2}O_{0.9}F$ pellets) sandwiched between two Pt bulk electrodes was performed at 600°C by applying a dc voltage of 5.0 V, which is higher than the decomposition voltage of the sample (Fig. 1.7). If the $La_{0.8}Mg_{0.2}O_{1-\delta}F$ solid is a pure F^- ion conductor, $La_{0.8}Mg_{0.2}O_{1-\delta}F$ at the cathodic side (pellet C) should be decompose by the following reaction to generate F^- ions:

$$La_{0.8}Mg_{0.2}O_{1-\delta}F + \frac{0.4+\delta}{2}O_2 + e^- \rightarrow \frac{2}{5}La_2O_3 + \frac{1}{5}MgO + F^- \qquad (1\text{-}3)$$

The generated F^- ions should conduct toward the anodic pellet (pellet A) through the middle pellet (pellet B) by the potential gradient. The F^- ions reached to the anodic pellet (pellet A) may react with $La_{0.8}Mg_{0.2}O_{1-\delta}F$ to form metal fluorides (LaF_3 and MgF_2) as the following reaction:

$$\frac{5}{9}La_{0.8}Mg_{0.2}O_{1-\delta}F + F^- \rightarrow \frac{4}{9}LaF_3 + \frac{1}{9}MgF_2 + \frac{5(1-\delta)}{18}O_2 + e^- \quad (1\text{-}4)$$

Since these reactions continuously occur during the electrolysis period, the weight changes depending on the amount of coulomb flowed in the circuit should be observed for each pellet, i.e. weight loss for pellet C and weight gain for pellet A, respectively. For the middle pellet, the weight change is not recognized theoretically. The theoretical weight change for each pellet was estimated from the amount of coulomb flowed the circuit during the electrolysis. Table 1.1 lists the theoretical and observed weight changes for each sample pellet by performing the modified Tubandt electrolysis for 12 h in atmospheric air. The observed weight changes for all sample pellets were well coincident with the theoretical ones within 8% error. Furthermore, since I have confirmed the generation of La_2O_3 and LaF_3 in the anodic sample pellet A and the cathodic sample pellet C, respectively, as shown in Fig. 1.8, it was clearly demonstrated that the above-described reactions occurred by applying dc voltage and that the charge carrier in the $La_{0.8}Mg_{0.2}O_{1-\delta}F$ solid was only F^- ions.

Table 1.1 Weight change of $La_{0.8}Mg_{0.2}O_{1-\delta}F$ pellets by the modified Tubandt electrolysis at 600°C for 12 h

Pellet	Theoretical weight change / mg	Observed weight change / mg	Observed / theoretical weight change
A ($La_{0.8}Mg_{0.2}O_{1-\delta}F$)	+0.73	+0.67	92.1%
B ($La_{0.8}Mg_{0.2}O_{1-\delta}F$)	0	−0.03	-
C ($La_{0.8}Mg_{0.2}O_{1-\delta}F$)	−0.73	−0.69	94.3%

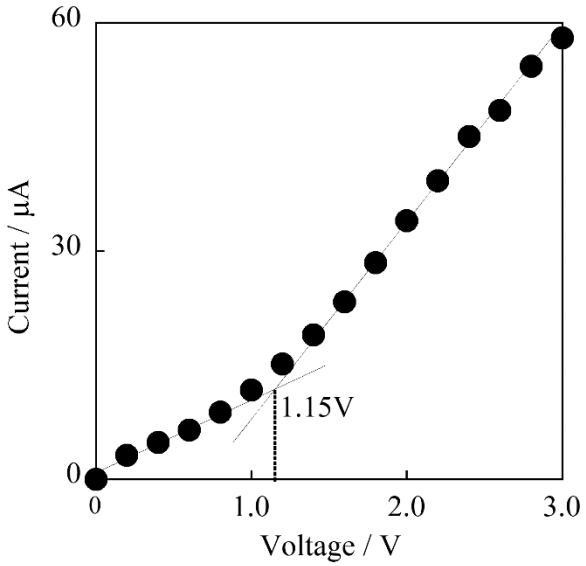


Figure 1.7 I-V curve for the $La_{0.8}Mg_{0.2}O_{1-\delta}F$ solid at 600°C in air.

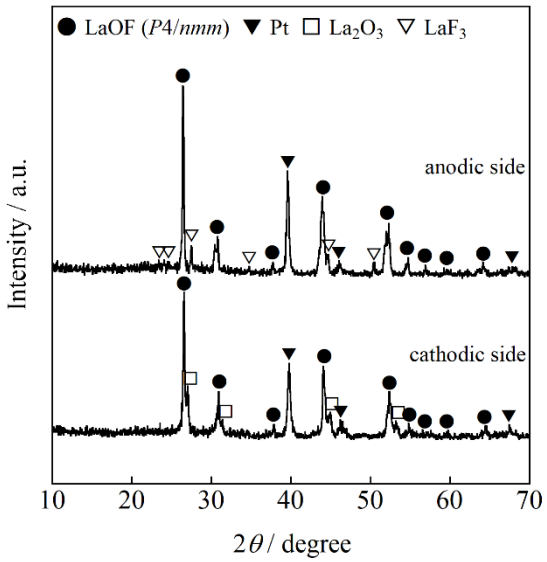


Figure 1.8 XRD patterns of the anodic and cathodic pellet after electrolysis at 600°C for 12 h.

1.4 Conclusions

To improve F^- ion conductivity with suppressing the phase transition of the LaOF solid, the Mg^{2+} ion doped LaOF, $La_{1-x}Mg_xO_{1-\delta}F$ were synthesized and the phase transition behavior and ion conducting property were investigated. The phase transition between tetragonal to trigonal structure was successfully suppressed by doping Mg^{2+} ion into the La^{3+} ion site of the LaOF solid, and the tetragonal LaOF structure was obtained stably for the samples with $x \geq 0.15$. Among the samples prepared, the $La_{0.8}Mg_{0.2}O_{0.9}F$ ($x = 0.2$) solid showed the highest F^- ion conductivity of 6.9×10^{-3} $S \cdot cm^{-1}$ which is ca. 46.5 times higher than that of LaOF ($x = 0$) solid at 800°C. The F^- ion conduction in the $La_{0.8}Mg_{0.2}O_{0.9}F$ solid was quantitatively demonstrated by the modified Tubandt electrolysis using three $La_{0.8}Mg_{0.2}O_{0.9}F$ pellets.

Chapter 2

Improvement of Fluoride Ion Conductivity by Strict Control of Lattice Volume and Fluoride Ion Concentration in Lanthanum Oxyfluoride.

2.1 Introduction

In Chapter 1, both the suppression of phase transition and the improvement of F^- ion conductivity has been successfully achieved for the LaOF solid by the partial substitution of divalent Mg^{2+} ion (0.103 nm (CN = 8) [29]) for the La^{3+} ion (0.130 nm (CN = 8) [29]) site to introduce the O^{2-} ion defects and lattice shrinkage. This result suggests that the formation of O^{2-} ion defect in the LaOF lattice, in other words, nonstoichiometric F/O ratio, suppresses phase transition and stabilizes tetragonal phase. Therefore, it is considered that the stabilization of the tetragonal phase of the LaOF with high F^- ion conductivity may also be achieved by introducing excess F^- ions into the LaOF lattice.

In this chapter, in order to investigate the phase transition behavior and the F^- ion conducting properties of LaOF containing excess F^- ions in the structure, the nonstoichiometric $LaO_{1-y}F_{1+2y}$ ($0 \leq y \leq 0.5$) were synthesized by intentionally varied F/O ratio. Furthermore, to improve the F^- ion conduction, I aimed to increase the amount of F^- ions in the lattice. Here, the La^{3+} ion (0.130 nm (CN = 8) [29]) site in LaOF was replaced with larger size of Sr^{2+} ion (0.140 nm (CN = 8) [29]) to form the $La_{1-x}Sr_xO_{0.6-0.5x-y}F_{1.8+2y}$ ($0 \leq x \leq 0.4$, $0 \leq y \leq 0.2$) solids, which is expected to have large lattice volume in addition to contain excess amount of F^- ions in the lattice.

2.2 Experimental Procedure

Two types of nonstoichiometric lanthanum oxyfluorides, non-doped $LaO_{1-y}F_{1+2y}$ ($0 \leq y \leq 0.5$) and Sr^{2+}-doped $La_{1-x}Sr_xO_{0.6-0.5x-y}F_{1.8+2y}$ ($0 \leq x \leq 0.4$, $0 \leq y \leq 0.2$), were synthesized by a solid-state reaction method. Stoichiometric amounts of La_2O_3, LaF_3, and $Sr(NO_3)_2$ were mixed in an agate motor under atmospheric air and calcined at 800°C for 12 h in synthetic air. The obtained powder was pelletized

and sintered under the same conditions. As same as Chapter 1, the characterizations of XRD measurement, TG-DTA, ac impedance measurement were performed for the synthesized samples. Modified Tubandt electrolysis was performed for the $LaO_{0.6}F_{1.8}$ and $La_{0.7}Sr_{0.3}O_{0.4}F_{1.9}$ solids by applying a dc voltage of 10 V at 300°C for 3-7 days in atmospheric air.

2.3 Results and Discussions

Figure 2.1 shows the XRD patterns of the $LaO_{1-y}F_{1+2y}$ ($0 \leq y \leq 0.5$) solids after the calcination at 800°C for 12 h in synthetic air. While the samples with $y \leq 0.4$ were the single-phase of tetragonal LaOF (*P*4/*nmm*) structure, the sample with $y = 0.5$ was the mixture of tetragonal LaOF (*P*4/*nmm*) and LaF_3. Figure 2.2 depicts the compositional dependence of the lattice volume for the $LaO_{1-y}F_{1+2y}$ solids obtained as the single-phase of tetragonal LaOF (*P*4/*nmm*) structure. The lattice volume linearly increased with increasing the amount of F^- ion (y) in the solids, suggesting that the $LaO_{1-y}F_{1+2y}$ ($0 \leq y \leq 0.4$) solids were formed a solid solution in which O^{2-} ion site was replaced by F^- ions and/or excess F^- ions were inserted into the interstitial position in the tetragonal LaOF lattice.

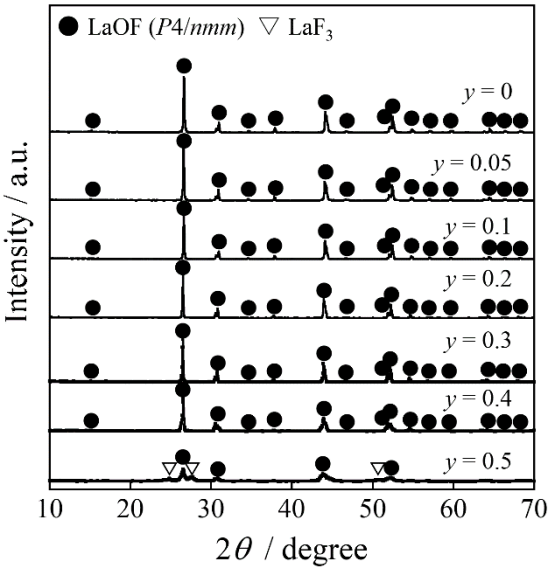


Figure 2.1 XRD pattern of the $LaO_{1-y}F_{1+2y}$ ($0 \leq y \leq 0.5$) solids.

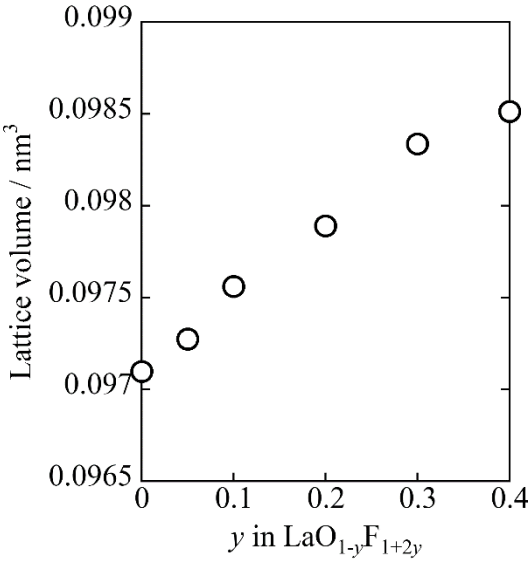


Figure 2.2 Compositional dependence of the lattice volume for the $LaO_{1-y}F_{1+2y}$ ($0 \leq y \leq 0.4$) solids.

Figure 2.3 presents the TG-DTA results for the $LaO_{1-y}F_{1+2y}$ ($0 \leq y \leq 0.4$) solids. As same as the $La_{1-x}Mg_xO_{1-\delta}F$ solids (in Chapter 1), the endothermic and exothermic DTA peaks with no weight change were observed around 500°C for the sample with $y = 0.05$. As clearly demonstrated in Chapter 1, since these peaks are by the phase transition between tetragonal and trigonal phases, it was concluded that the $LaO_{0.95}F_{1.1}$ ($y = 0.05$) also showed the phase transition. In contrast, such a DTA peaks suggesting phase transition was disappeared in the samples with $y \geq 0.1$. Moreover, no structural change in the samples with $y \geq 0.1$ was confirmed by the in-situ XRD measurement (The result for the sample with $y = 0.1$ is shown in Figure 2.4.), revealing that the phase transition was successfully suppressed for the $LaO_{1-y}F_{1+2y}$ solids with the F^- ion content (y) over 0.1. From these results, it was found that excess amount of F^- ions which exist interstitial sites in the tetragonal LaOF lattice may prohibit the displacement of the lattice constituent elements, while the amount of F^- ion in the sample with $y = 0.05$ is too small to suppress the phase transition.

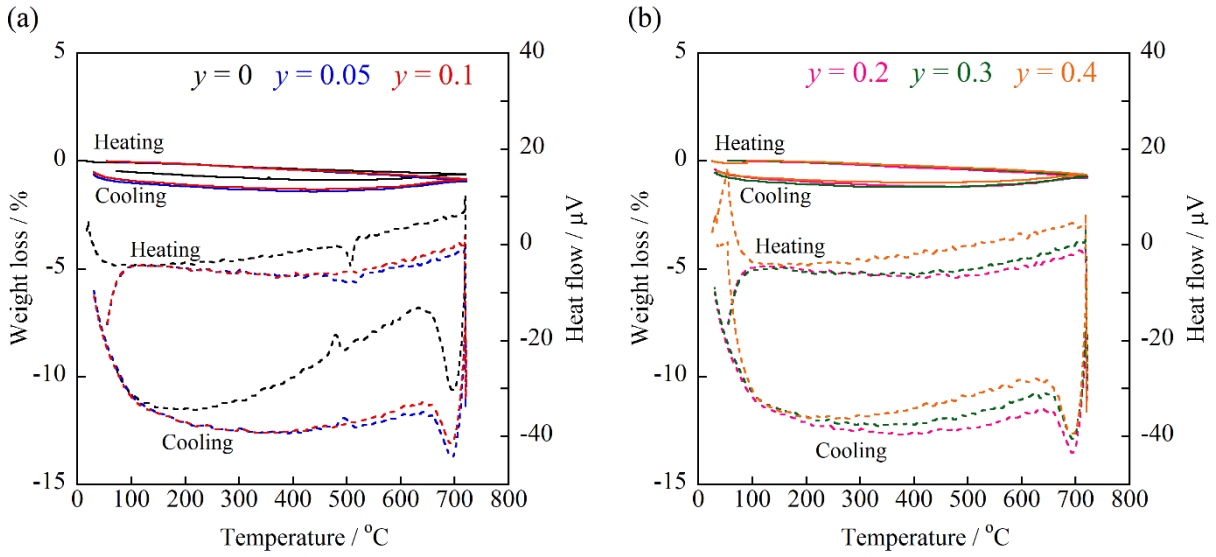


Figure 2.3 TG (solid line) and DTA (dotted line) curves for the $LaO_{1-y}F_{1+2y}$ ((a) $0 \leq y \leq 0.1$, (b) $0.2 \leq y \leq 0.4$) solids.

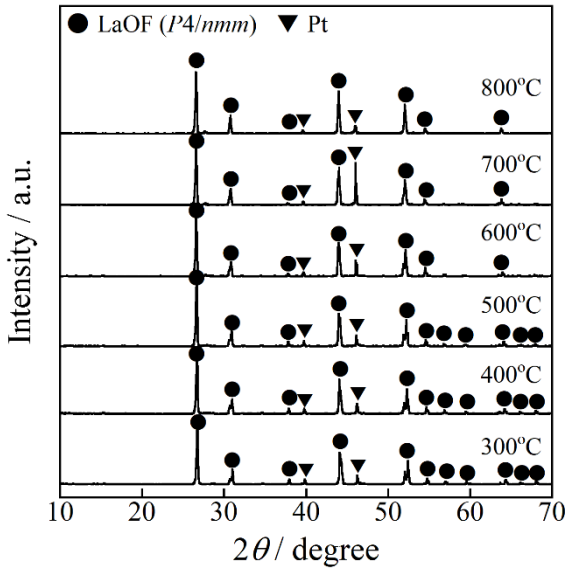


Figure 2.4 In-situ XRD patterns of the $LaO_{0.9}F_{1.2}$ ($y = 0.1$) solids between 300 and 800°C in cooling step.

Figure 2.5 shows the temperature dependence of the ac conductivity for the $LaO_{1-y}F_{1+2y}$ ($0 \leq y \leq 0.4$) solids obtained as the single-phase sample with the corresponding data for the reported stoichiometric LaOF having tetragonal and trigonal structure [27]. While the samples with $y \leq 0.05$ which exhibited phase transition showed the gradient change in the temperature dependence of the conductivity, such a gradient change was not observed in the samples with $y \geq 0.1$ whose structure was stabilized as the tetragonal one. This result also supports that the phase transition is suppressed by introduction of F^- ions into the tetragonal LaOF lattice. Figure 2.6 shows the compositional dependencies of the ac conductivity at 800°C and the activation energy for the F^- ion conduction in the tetragonal LaOF lattice for the $LaO_{1-y}F_{1+2y}$ ($0 \leq y \leq 0.4$) solids. Both the increase of the F^- ion conductivity and the decrease of the activation energy were observed with increasing the F^- ion concentration. This symmetrical behavior is probably due to acceleration of the F^- ion conduction in the LaOF lattice by shortening the distance between F^- ions and increasing the F^- ion diffusion route owing to the existence of excess F^- ions into the interstitial site and/or O^{2-} ion site. Among the samples, the $LaO_{0.6}F_{1.8}$ ($y = 0.4$) solid showed the highest conductivity of 2.7×10^{-5} S·cm^{-1} at 300°C which is

approximately 1000 times higher than that of the LaOF solid.

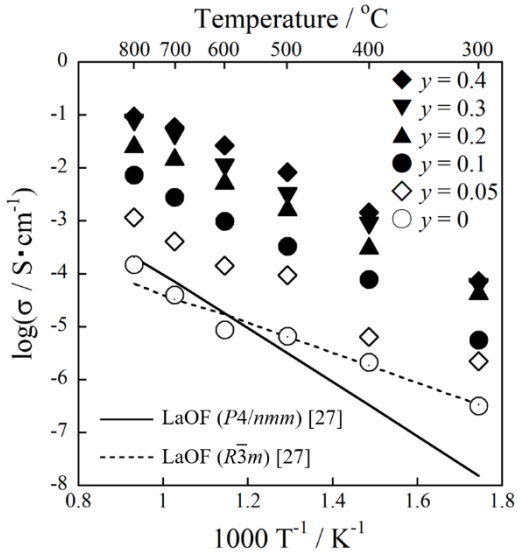


Figure 2.5 Temperature dependencies of the ionic conductivity for the $LaO_{1-y}F_{1+2y}$ ($0 \leq y \leq 0.4$) solids with the corresponding data for the previously reported tetragonal and trigonal LaOF solids [27].

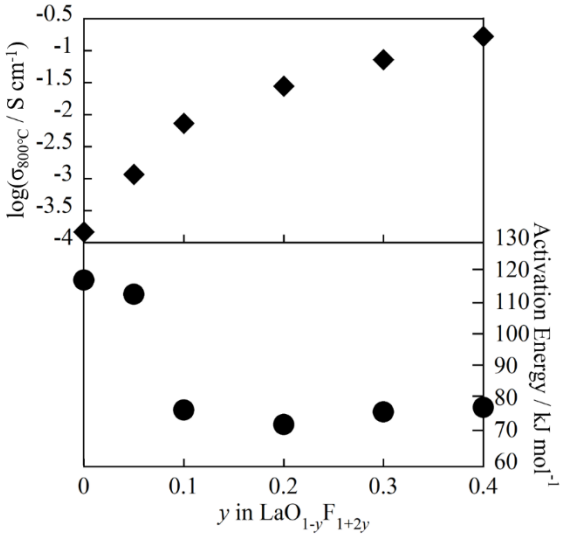


Figure 2.6 Compositional dependencies of the ionic conductivity at 800°C and the activation energy for F^- ion conduction in the tetragonal LaOF structure for the nonstoichiometric $LaO_{1-y}F_{1+2y}$ solids.

The F^- ion migration in the $LaO_{0.6}F_{1.8}$ solid was investigated by modified Tubandt electrolysis method as same as the Chapter 1. The electrolysis was performed at 300℃ using sintered three $LaO_{0.6}F_{1.8}$ pellets by applying a dc voltage of 10 V, which is higher than decomposition voltage (1.0 V) of the sample. As same as the case for the $La_{0.8}Mg_{0.2}O_{1-\delta}F$ (Chapter 1), the following reactions should occur at the cathodic and anodic samples:

(Cathodic $LaO_{0.6}F_{1.8}$ pellet)

$$LaO_{0.6}F_{1.8} + \frac{9}{20}O_2 + \frac{9}{5}e^- \rightarrow \frac{1}{2}La_2O_3 + \frac{9}{5}F^- \quad (2\text{-}1)$$

(Anodic $LaO_{0.6}F_{1.8}$ pellet)

$$LaO_{0.6}F_{1.8} + \frac{6}{5}F^- \rightarrow LaF_3 + \frac{3}{10}O_2 + \frac{6}{5}e^- \quad (2\text{-}2)$$

The reaction at the anodic pellet, of which excess amount of F doping into LaOF structure generates LaF_3, can be also speculated from the XRD result for the sample with $y = 0.5$, which is obtained as a

two-phase mixture of LaOF and LaF_3 (see Figure 2.1). Table 2.1 tabulates the weight change of each sample pellet observed by modified Tubandt electrolysis for 7 days with theoretical one estimated from the electrolysis condition (current and time). Although the observed weight change of the pellet C was slightly smaller than theoretical one, the weight gain for pellet A was observed with an error of less than 5%. Furthermore, I have also confirmed that LaF_3 and La_2O_3 were generated at the surface of electrolyzed pellets A and C, respectively, by the XRD measurement (Figure 2.7). From the Tubandt electrolysis experiment, only F^- ion migration was quantitative demonstrated for the $LaO_{0.6}F_{1.8}$ solid.

Table 2.1 Weight change of $LaO_{0.6}F_{1.8}$ pellets after modified Tubandt electrolysis at 300℃ for 7 days

Pellet	Theoretical weight change / mg	Observed weight change / mg	Observed / theoretical weight change
A ($LaO_{0.6}F_{1.8}$)	+0.22	+0.21	95.4%
B ($LaO_{0.6}F_{1.8}$)	0	+0.01	-
C ($LaO_{0.6}F_{1.8}$)	−0.22	−0.19	86.4%

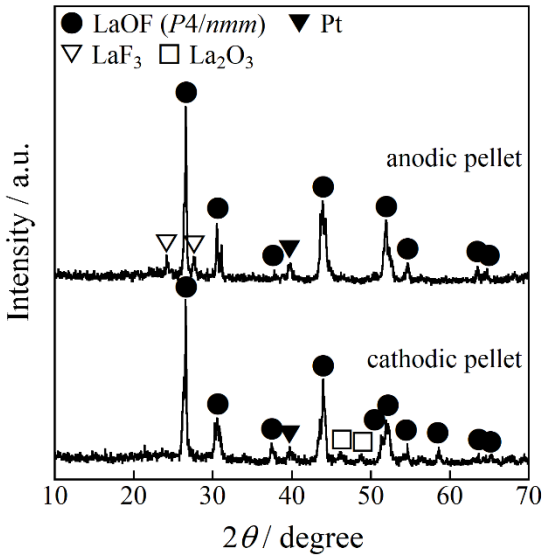


Figure 2.7 XRD patterns of the anodic and cathodic pellet after electrolysis at 300℃ for 7 days.

These results indicate that the improvement of the F^- ion conductivity with prohibiting the phase

transition for the LaOF solid can be also achieved by introducing both O^{2-} ion defect and excess amount of F^- ions into the LaOF lattice. Therefore, it is expected to further improve the F^- ion conductivity by the optimization of the O and F composition in the solid. To introduce additional O^{2-} ion defects into the LaOF structure, divalent Sr^{2+} ion was doped into the La^{3+} ion site in the $LaO_{0.6}F_{1.8}$ solid and the $La_{1-x}Sr_xO_{0.6-0.5x}F_{1.8}$ ($0 \leq x \leq 0.4$) solids were synthesized. Figure 2.8 depicts the XRD patterns of the $La_{1-x}Sr_xO_{0.6-0.5x}F_{1.8}$ ($0 \leq x \leq 0.4$) solids obtained by the calcination at 800°C for 12 h in air. All the samples obtained were the single-phase samples with the tetragonal LaOF structure, and the lattice volume for the $La_{0.6}Sr_{0.4}O_{0.4}F_{1.8}$ ($x = 0.4$) was smaller than those for the samples with $x \leq 0.3$ while the lattice volume for the samples with $x \leq 0.3$ was linearly increased with increasing Sr^{2+} ion content (x) (Figure 2.9). From this result, it was clear that the larger Sr^{2+} ion (0.140 nm (CN = 8) [29]) partially replaced La^{3+} ion (0.130 nm (CN = 8) [29]) site in the tetragonal LaOF structure for the samples with $x \leq 0.3$ and the single-phase of $La_{0.6}Sr_{0.4}O_{0.4}F_{1.8}$ solid cannot form due to the large amount of O^{2-} ion defect for maintain the LaOF phase.

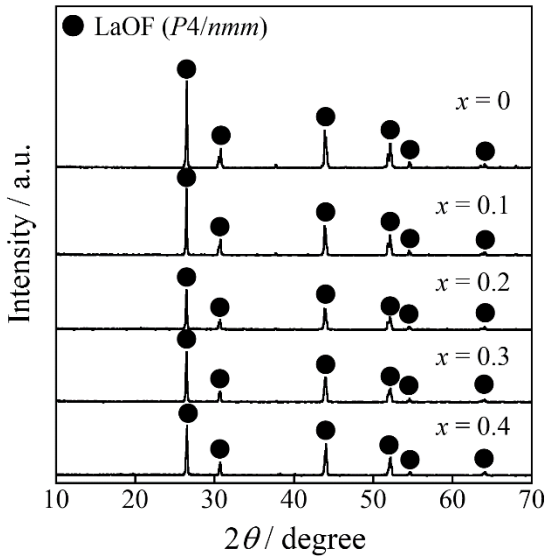


Figure 2.8 XRD patterns of the $La_{1-x}Sr_xO_{0.6-0.5x}F_{1.8}$ ($0 \leq x \leq 0.4$) solids.

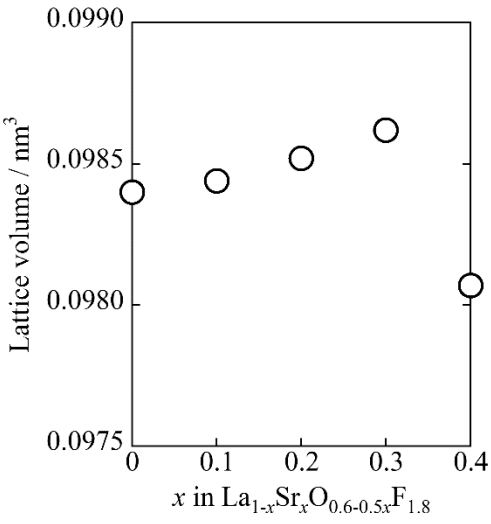


Figure 2.9 Compositional dependence of the lattice volume for the $La_{1-x}Sr_xO_{0.6-0.5x}F_{1.8}$ ($0 \leq x \leq 0.4$) solids.

Figure 2.10 shows the compositional dependencies of the ac conductivity at 300℃ and the activation energy for F^- ion migration for the $La_{1-x}Sr_xO_{0.6-0.5x}F_{1.8}$ ($0 \leq x \leq 0.4$) solids. Both the increase of conductivity and the decrease of activation energy were observed with increasing the Sr^{2+} ion concentration in the $La_{1-x}Sr_xO_{0.6-0.5x}F_{1.8}$ solids for the single-phase sample region with $x \leq 0.3$. This is probably due to the expansion of F^- ion conducting pathway owing to the lattice volume expansion which is caused by the generation of O^{2-} ion vacancies. On the other hand, the conductivity of the sample with $x = 0.4$ drastically decreased because of the impurity phase.

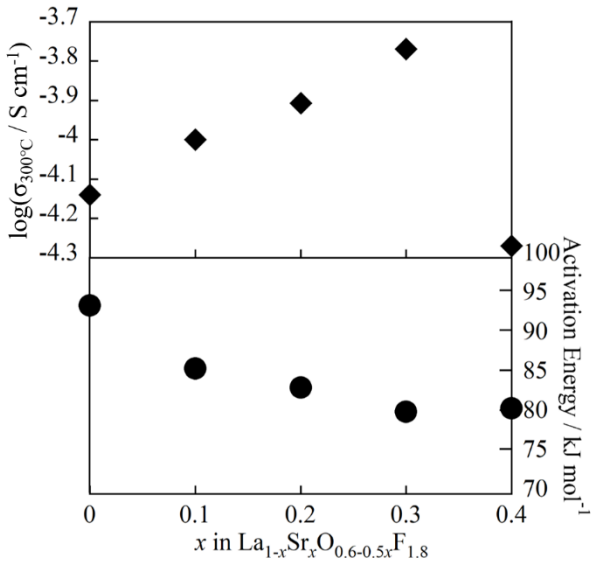


Figure 2.10 Compositional dependencies of ionic conductivity at 300 °C and activation energy for the ionic conduction in the $La_{1-x}Sr_xO_{0.6-0.5x}F_{1.8}$ solids.

Since the $La_{0.7}Sr_{0.3}O_{0.45}F_{1.8}$ solid was found to show the highest conductivity, the $La_{0.7}Sr_{0.3}O_{0.45-y}F_{1.8+2y}$ ($0 < y \leq 0.15$) solids were synthesized to optimize the F/O ratio for the Sr-doped LaOF. Figure 2.11 presents the XRD patterns of the $La_{0.7}Sr_{0.3}O_{0.45-y}F_{1.8+2y}$ ($0 < y \leq 0.15$) solids obtained by calcination at 800℃ for 12 h in synthetic air. Although the sample with $y = 0.05$ possessed a single-phase of tetragonal LaOF structure like $La_{0.7}Sr_{0.3}O_{0.45}F_{1.8}$, the sample with $y > 0.1$ were the two-phase mixture of tetragonal LaOF structure and SrF_2. The lattice volume for the obtained samples calculated from their XRD peak angles were depicted in Figure 2.12. The single-phase $La_{0.7}Sr_{0.3}O_{0.4}F_{1.9}$ ($y = 0.05$)

solid shows larger lattice volume compared with the $La_{0.7}Sr_{0.3}O_{0.45}F_{1.8}$ solid, but the lattice volume of the samples with $y \geq 0.1$ decreased with y. This trend in lattice volume change suggests that the solid, whose F^- ion content exceeds the limiting composition that can stably retain the LaOF structure, decomposed to form SrF_2 as an impurity phase. From these results, further F^- ions can be introduced into the LaOF lattice by doping Sr^{2+} ion into the La^{3+} ion site to generate much amount of O^{2-} ion defects.

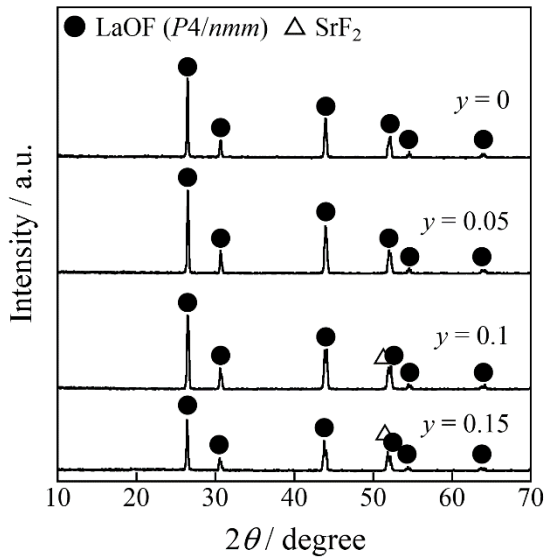


Figure 2.11 XRD patterns of the $La_{0.7}Sr_{0.3}O_{0.45-y}F_{1.8+2y}$ ($0 < y \leq 0.15$) solids.

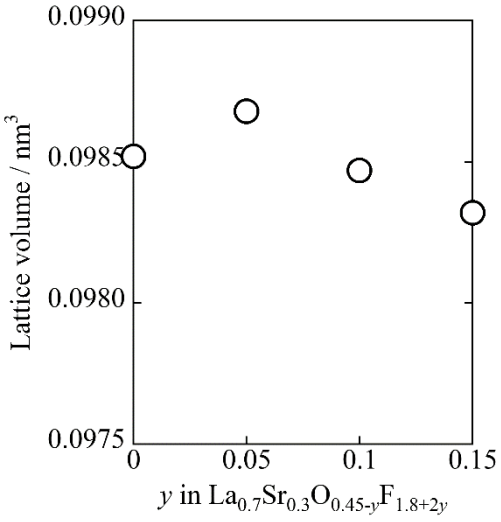


Figure 2.12 Compositional dependence of the lattice volume for the $La_{0.7}Sr_{0.3}O_{0.45-y}F_{1.8+2y}$ ($0 < y \leq 0.15$) solids.

Figure 2.13 shows the compositional dependencies of the ac conductivity at 300°C and the activation energy of F^- ion conduction for the $La_{0.7}Sr_{0.3}O_{0.45-y}F_{1.8+2y}$ ($0 < y \leq 0.15$) solids. The $La_{0.7}Sr_{0.3}O_{0.4}F_{1.9}$ ($y = 0.05$) solid showed higher conductivity and lower activation energy than those for the $La_{0.7}Sr_{0.3}O_{0.45}F_{1.8}$ ($y = 0$) solid. In contrast, the samples with $y > 0.05$ showed lower conductivity and higher activation energy than those for the $La_{0.7}Sr_{0.3}O_{0.4}F_{1.9}$ ($y = 0.05$) solid. These results clearly indicate that the $La_{0.7}Sr_{0.3}O_{0.4}F_{1.9}$ ($x = 0.3$, $y = 0.05$) solid having the solid solubility composition showed the highest conductivity (2.9×10^{-4} $S\cdot cm^{-1}$), which is ca. 930 times higher than that of

stoichiometric LaOF at 300°C, and the lowest activation energy (79.0 kJ·mol^{-1}) among the prepared samples.

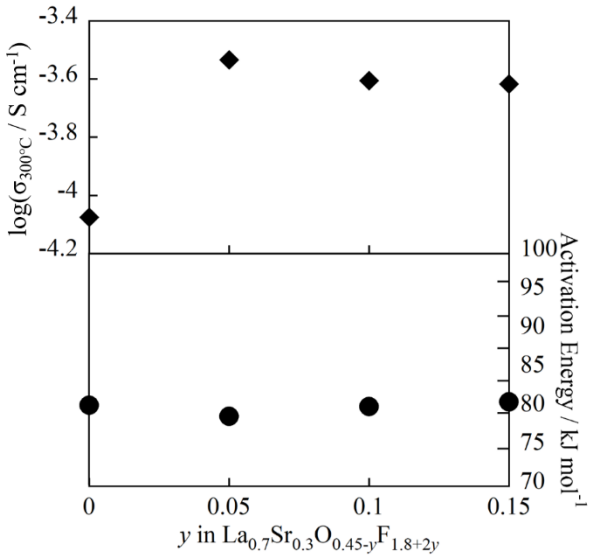


Figure 2.13 Compositional dependencies of ionic conductivity at 300°C and activation energy for the ionic conduction in $La_{0.7}Sr_{0.3}O_{0.45-y}F_{1.8+2y}$ ($0 < y \leq 0.15$) solids.

The F^- ion migration in the $La_{0.7}Sr_{0.3}O_{0.4}F_{1.9}$ (x = 0.3, y = 0.05) solid possessed the highest conductivity among the prepared samples was demonstrated by the modify Tubandt electrolysis. The electrolysis was done at 300°C by applying 10V dc voltage (The decomposition voltage of the $La_{0.7}Sr_{0.3}O_{0.4}F_{1.9}$ (x = 0.3, y = 0.05) solid was confirmed to be 1.4 V.). Here, I used $LaO_{0.6}F_{1.8}$ pellet as the cathodic pellet C instead of $La_{0.7}Sr_{0.3}O_{0.4}F_{1.9}$ solid, because high resistivity SrO that may form during the electrolysis prevents a continuous smooth current flow through the samples, i.e., a smooth F^- ion supply to the anodic pellet. Table 2.2 lists the weight change of each pellet after modified Tubandt electrolysis for 3 days in the atmospheric air with the theoretical weight change calculated from the amount of coulomb flowing in the circuit during electrolysis. Over 95% weight changes of theoretical value were observed both in the pellets A and C with no weight change in the pellet B, indicating that only F^- ions migrated in the $La_{0.7}Sr_{0.3}O_{0.4}F_{1.9}$ (x = 0.3, y = 0.05) solid.

Table 2.2 Weight change of $La_{0.7}Sr_{0.3}O_{0.4}F_{1.9}$ and $LaO_{0.6}F_{1.8}$ pellets after modified Tubandt electrolysis at 300℃ for 3 days

Pellet	Theoretical weight change / mg	Observe weight change / mg	Observe / theoretical weight change
A ($La_{0.7}Sr_{0.3}O_{0.4}F_{1.9}$)	+0.31	+0.30	96.8%
B ($La_{0.7}Sr_{0.3}O_{0.4}F_{1.9}$)	0	+0.02	-
C ($LaO_{0.6}F_{1.8}$)	−0.31	−0.30	96.8%

2.4 Conclusions

In this chapter, I aimed to investigate the phase transition behavior and the F^- ion conducting properties of the nonstoichiometric lanthanum oxyfluorides, $LaO_{1-y}F_{1+2y}$ ($0 \le y \le 0.5$). Similar to the case for the $La_{1-x}Mg_xO_{1-\delta}F$ solids (Chapter 1), the phase transition was successfully suppressed by varying the F/O ratio in the LaOF. Furthermore, F^- ion conductivity was improved by increasing the F^- ion content (y) and the $LaO_{0.6}F_{1.8}$ ($y = 0.4$) solid showed the highest F^- ion conductivity (2.7×10^{-5} $S \cdot cm^{-1}$ at 300℃) among the $LaO_{1-y}F_{1+2y}$ solids. To obtain an appropriate circumstance for high F^- ion conduction, the $La_{1-x}Sr_xO_{0.6-0.5x-y}F_{1.8+2y}$ ($0 \le x \le 0.4$, $0 \le y \le 0.2$) solids were synthesized by doping larger Sr^{2+} ion into the La^{3+} ion site. Lattice expansion and the generation of additional O^{2-} ion defects resulted in the introduction of large amount of F^- ions into the LaOF structure. Among the solid prepared, the $La_{0.7}Sr_{0.3}O_{0.4}F_{1.9}$ ($x = 0.3$, $y = 0.05$) solid, which has the largest lattice volume and the highest F^- ion concentration in the lattice showed the highest F^- ion conductivity which is ca. 930 times higher than that of stoichiometric LaOF at 300℃.

Chapter 3

Crystal Phase and Fluoride Ion Conducting Behavior of Nonstoichiometric Rare-earth Oxyfluorides.

3.1 Introduction

In Chapters 1 and 2, I achieved the enhancement of F^- ion conductivity and the suppression of phase transition in LaOF by controlling the lattice size and anion defect content. However, there are no reports on the relationship between the crystal phase and ionic conductivity for other rare earth oxyfluorides (*R*OFs) than LaOF. Moreover, since the factors defining the crystal phase of the *R*OFs are not clear, nonstoichiometric $RO_{1-y}F_{1+2y}$ ($0 \leq y \leq 0.4$; *R* = La, Pr, Nd, Sm, Eu, Gd, Tb, Dy, Ho, Er, Tm, and Yb) solids were synthesized and their structural properties including phase transition were systematically investigated to reveal the crystal phase and the conducting properties of *R*OFs.

3.2 Experimental Procedure

Nonstoichiometric *R*OFs ($RO_{1-y}F_{1+2y}$ ($0 \leq y \leq 0.4$; *R* = La, Pr, Nd, Sm, Eu, Gd, Tb, Dy, Ho, Er, Tm, and Yb)) solids were synthesized by a solid-state reaction method. Stoichiometric amount of rare-earth oxide (R_2O_3 (*R* = La, Nd, Sm, Eu, Gd, Dy, Ho, Er, Tm, and Yb), Pr_6O_{11}, Tb_4O_7) and rare-earth fluoride RF_3 were mixed in an agate motor and calcined at 800℃ for 12 h in synthetic air. After calcination, the resulting powders were formed into pellets and sintered under the same condition as the calcination.

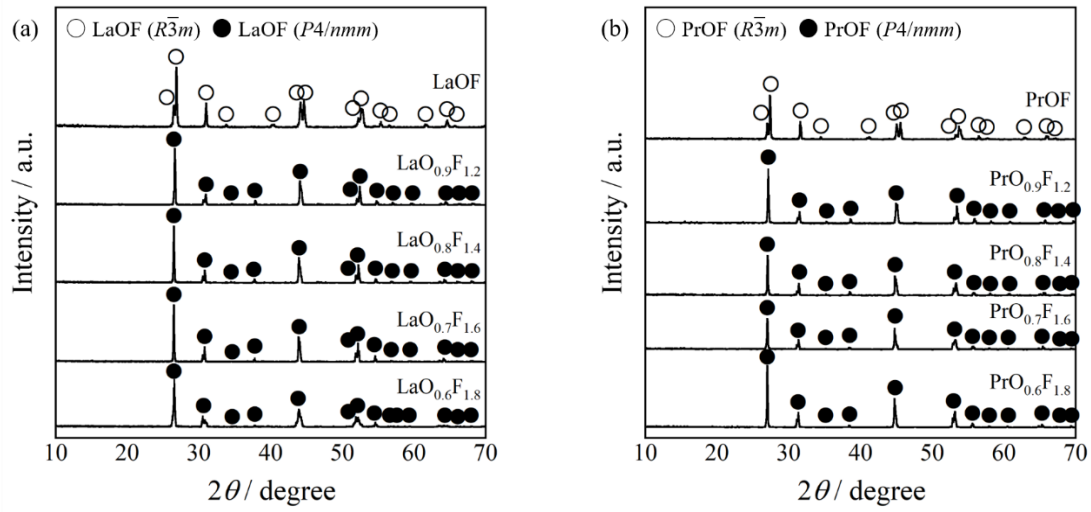
The synthesized samples were identified by X-ray powder diffraction (XRD; SmartLab, Rigaku) with Cu-Kα radiation (40 kV, 40 mA) using a step scanning method in the 2θ range of 10–70° with a step width of 0.02°. The obtained patterns were refined by Rietveld method with RIETAN-FP program [30] to determine the crystallographic data of the samples [31-34].

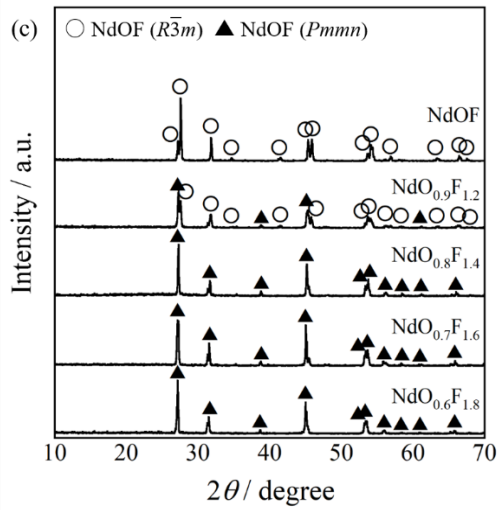
Ac conductivity of the sintered sample pellet with forming Pt thin films on both surfaces by spattering was measured using the complex impedance method in the frequency range of 1 Hz to 13

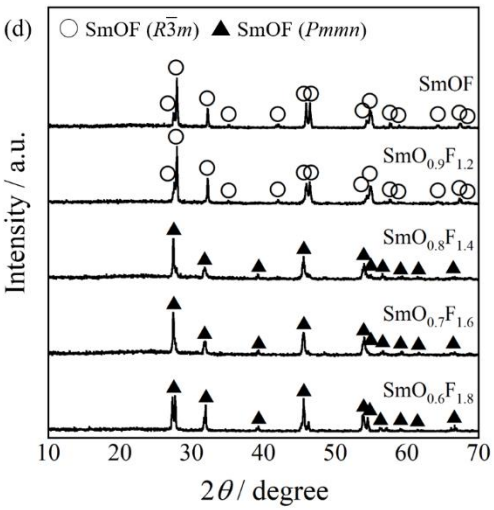
MHz (1260 Impedance/Gain-Phase Analyzer, Solartron) at temperature range from 300 to 800℃ in air.

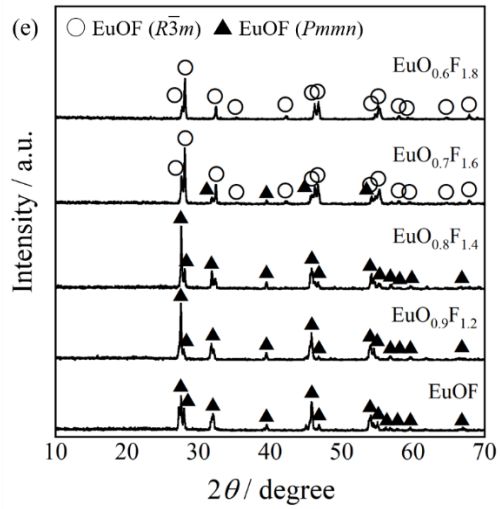
3.3 Results and Discussions

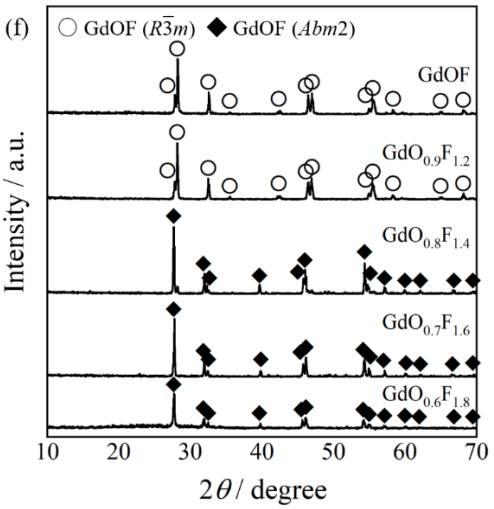
Figure 3.1 presents the X-ray powder diffraction (XRD) patterns of the $RO_{1-y}F_{1+2y}$ (R = La, Pr, Nd, Sm–Yb; $0 \le y \le 0.4$) solids. Although some samples were identified as two-phase mixture, main crystalline phase formed changed with the rare-earth element and composition. Figure 3.2 summarizes the crystal structure at room temperature for the $RO_{1-y}F_{1+2y}$ (R = La, Pr, Nd, Sm–Yb; $0 \le y \le 0.4$) solids formed by the calcination at 800℃ for 12 h in air as a function of R^{3+} ionic radius. For the stoichiometric ROFs (y = 0.0), the stable crystalline phase was found to be a trigonal structure ($R\bar{3}m$), except for YbOF, and the trigonal phase was also formed for the nonstoichiometric samples except for $LaO_{1-y}F_{1+2y}$ and $PrO_{1-y}F_{1+2y}$ ($0.1 \le y \le 0.4$) solids. Furthermore, it was confirmed that the compositional range where the $R\bar{3}m$ phase retained increased with decreasing the R^{3+} ionic size of the $RO_{1-y}F_{1+2y}$ solids. In contrast, nonstoichiometric $RO_{1-y}F_{1+2y}$ ($0.1 \le y \le 0.4$) solids hold various structures depending on rare-earth species; tetragonal ($P4/nmm$) for R = La, Pr, orthorhombic ($Pmmn$) for R = Nd, Sm, Eu, and orthorhombic ($Abm2$) phases for R = Gd, Tb, Dy Ho, Er, Tm, Yb.

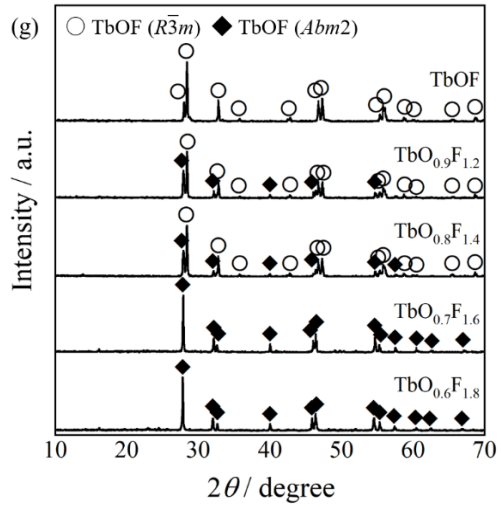


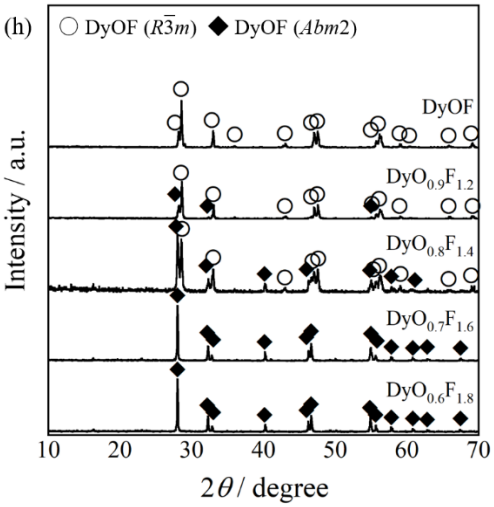

(c)
○ NdOF ($R\bar{3}m$) ▲ NdOF ($Pmmn$)
NdOF
$NdO_{0.9}F_{1.2}$
$NdO_{0.8}F_{1.4}$
$NdO_{0.7}F_{1.6}$
$NdO_{0.6}F_{1.8}$
Intensity / a.u.
10 20 30 40 50 60 70
2θ / degree


(d)
○ SmOF ($R\bar{3}m$) ▲ SmOF ($Pmmn$)
SmOF
$SmO_{0.9}F_{1.2}$
$SmO_{0.8}F_{1.4}$
$SmO_{0.7}F_{1.6}$
$SmO_{0.6}F_{1.8}$
Intensity / a.u.
10 20 30 40 50 60 70
2θ / degree


(e)
○ EuOF ($R\bar{3}m$) ▲ EuOF ($Pmmn$)
$EuO_{0.6}F_{1.8}$
$EuO_{0.7}F_{1.6}$
$EuO_{0.8}F_{1.4}$
$EuO_{0.9}F_{1.2}$
EuOF
Intensity / a.u.
10 20 30 40 50 60 70
2θ / degree


(f)
○ GdOF ($R\bar{3}m$) ◆ GdOF ($Abm2$)
GdOF
$GdO_{0.9}F_{1.2}$
$GdO_{0.8}F_{1.4}$
$GdO_{0.7}F_{1.6}$
$GdO_{0.6}F_{1.8}$
Intensity / a.u.
10 20 30 40 50 60 70
2θ / degree


(g)
○ TbOF ($R\bar{3}m$) ◆ TbOF ($Abm2$)
TbOF
$TbO_{0.9}F_{1.2}$
$TbO_{0.8}F_{1.4}$
$TbO_{0.7}F_{1.6}$
$TbO_{0.6}F_{1.8}$
Intensity / a.u.
10 20 30 40 50 60 70
2θ / degree


(h)
○ DyOF ($R\bar{3}m$) ◆ DyOF ($Abm2$)
DyOF
$DyO_{0.9}F_{1.2}$
$DyO_{0.8}F_{1.4}$
$DyO_{0.7}F_{1.6}$
$DyO_{0.6}F_{1.8}$
Intensity / a.u.
10 20 30 40 50 60 70
2θ / degree

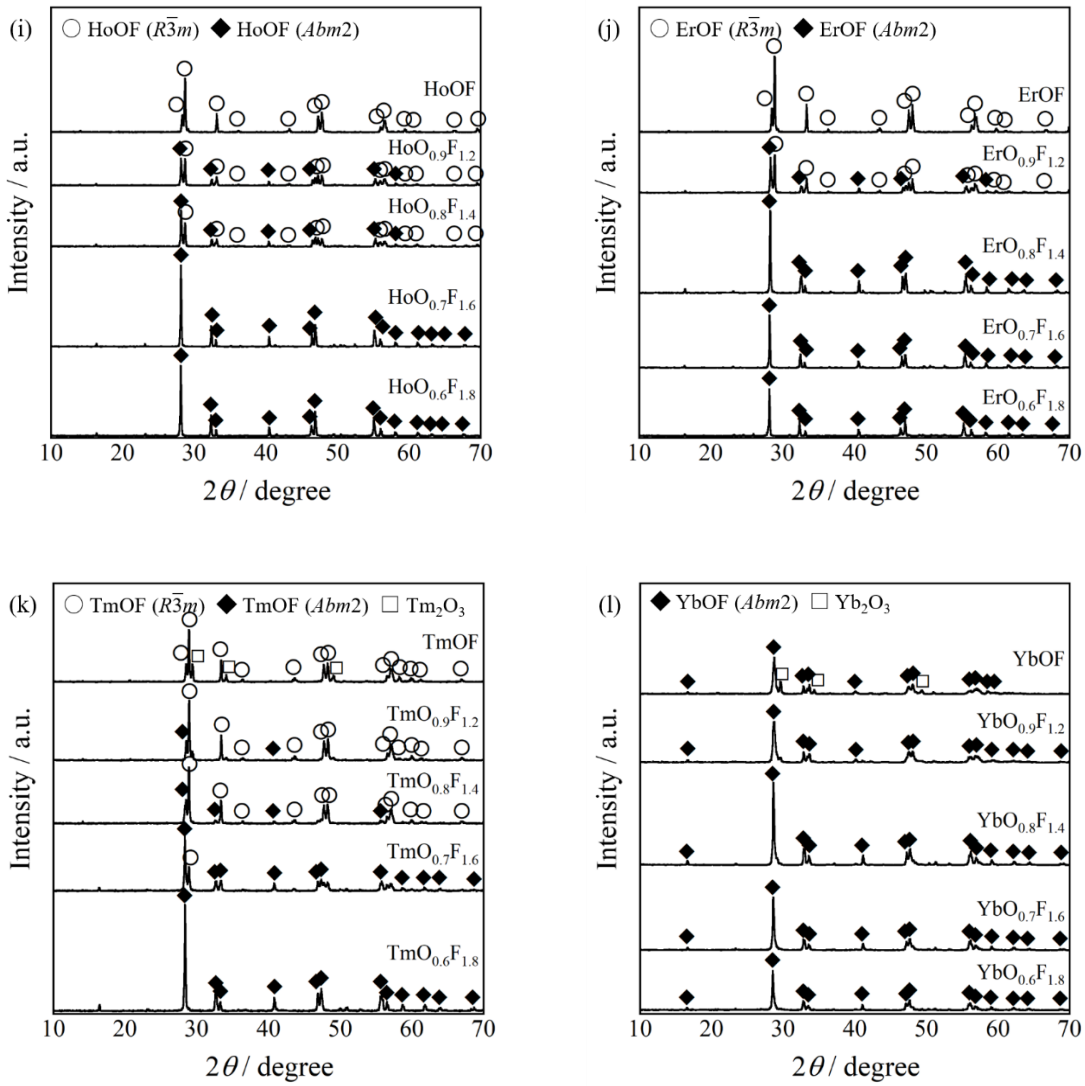


Figure 3.1 XRD patterns of the $RO_{1-y}F_{1+2y}$ ($0 \leq y \leq 0.4$; R = (a) La, (b) Pr, (c) Nd, (d) Sm, (e) Eu, (f) Gd, (g) Tb, (h) Dy, (i) Ho, (j) Er, (k) Tm, (l) Yb) solids.

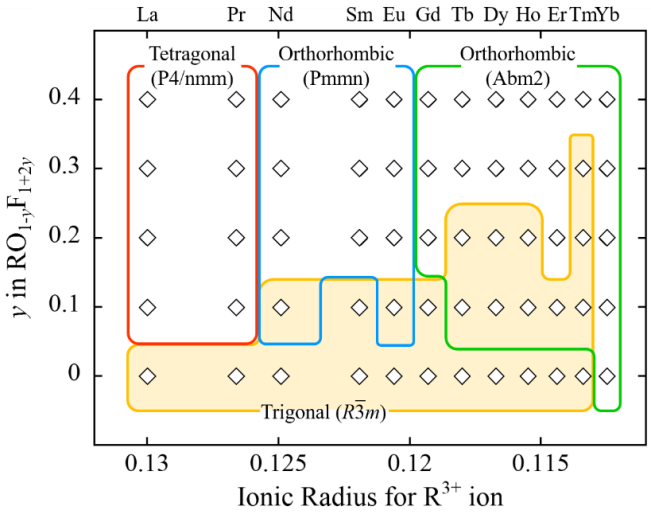


Figure 3.2 Crystal structure formed at room temperature for the $RO_{1-y}F_{1+2y}$ (R = La, Pr, Nd, Sm-Yb; $0 \leq y \leq 0.4$) solids.

To investigate the factors defining the crystalline phase of $RO_{1-y}F_{1+2y}$ solids, Rietveld refinement was performed by means of the RIETAN-FP program [30]. Figure 3.3 and Table 3.1 show the Rietveld refinement results for the stoichiometric *R*OFs (*R* = La, Nd, Eu, Gd, Ho, Er; $y = 0.0$). The measured patterns of all samples were assigned well to those of the trigonal *R*OF structure with small R_{wp} and S ($= R_{wp}/R_e$) values. Figure 3.4 illustrates the unit cell and RO_4F_4 local unit of the trigonal *R*OF structure, which are expected from the Rietveld refinement. As listed in Table 3.1, *R*OF solids have only one O and one F crystallographic site in the unit cell, respectively, indicating that all O or F atoms drawn in Figure 3.4(a) are crystallographically equivalent. Therefore, we distinguish them as *X*(1) and *X*(2) (*X* = O or F) to discuss the local structural changes of the RO_4F_4 unit (Figure 3.4(b)). Here, I labeled *X*(1) as the atom located in the *c*-axis direction viewed from the rare-earth atom, and the other atoms are as *X*(2). Table 3.2 tabulates the distances between *R*, O, and F atoms, which are calculated from the Rietveld refinement result, and the distance ratio of *R*–*X*(1) to *R*–*X*(2) ($d_{R-X(1)}/d_{R-X(2)}$). All the *R*–*X* (*X* = F, O) distances decreased monotonically as the R^{3+} ionic radius decreased. However, its contraction was anisotropic: the ratio of *R*–F(1) to *R*–F(2) ($d_{R-F(1)}/d_{R-F(2)}$) decreased as the R^{3+} ion size decreased although the ratio of the *R*–O(1) to *R*–O(2) distance ($d_{R-O(1)}/d_{R-O(2)}$) was almost constant regardless of the R^{3+} ion species. Such anisotropic contraction of the RO_4F_4 unit suggests that the F(1) atoms are displaced in the *c*-axis direction (Figure 3.4(c)). Moreover, it was found that the F(2)–F(2) distance ($d_{F(2)-F(2)}$) is almost the same as the O(2)–O(2) one ($d_{O(2)-O(2)}$), which is approximately equal to the lattice parameter *a* for each *R*OF, whereas F^- ion (0.117 nm (CN = 4) [29]) is smaller than O^{2-} ion (0.124 nm (CN = 4) [29]). This result means that the repulsion between F atoms is smaller than that between O atoms and, as a result, only F atoms are displaced significantly in the *c*-axis direction with shortening the *R*–F–*R* distance. However, this anisotropic distortion related to the decrease in ionic radius of R^{3+} is considered to expand the compositional range that retains the $R\bar{3}m$ phase of nonstoichiometric $RO_{1-y}F_{1+2y}$ solids with smaller R^{3+} ions. While *R*OFs with smaller rare-earth elements contains larger local distortions in the RO_4F_4 unit, this effect may have been eased by the introduction of additional F atoms in the structure, thereby enlarging the lattice.

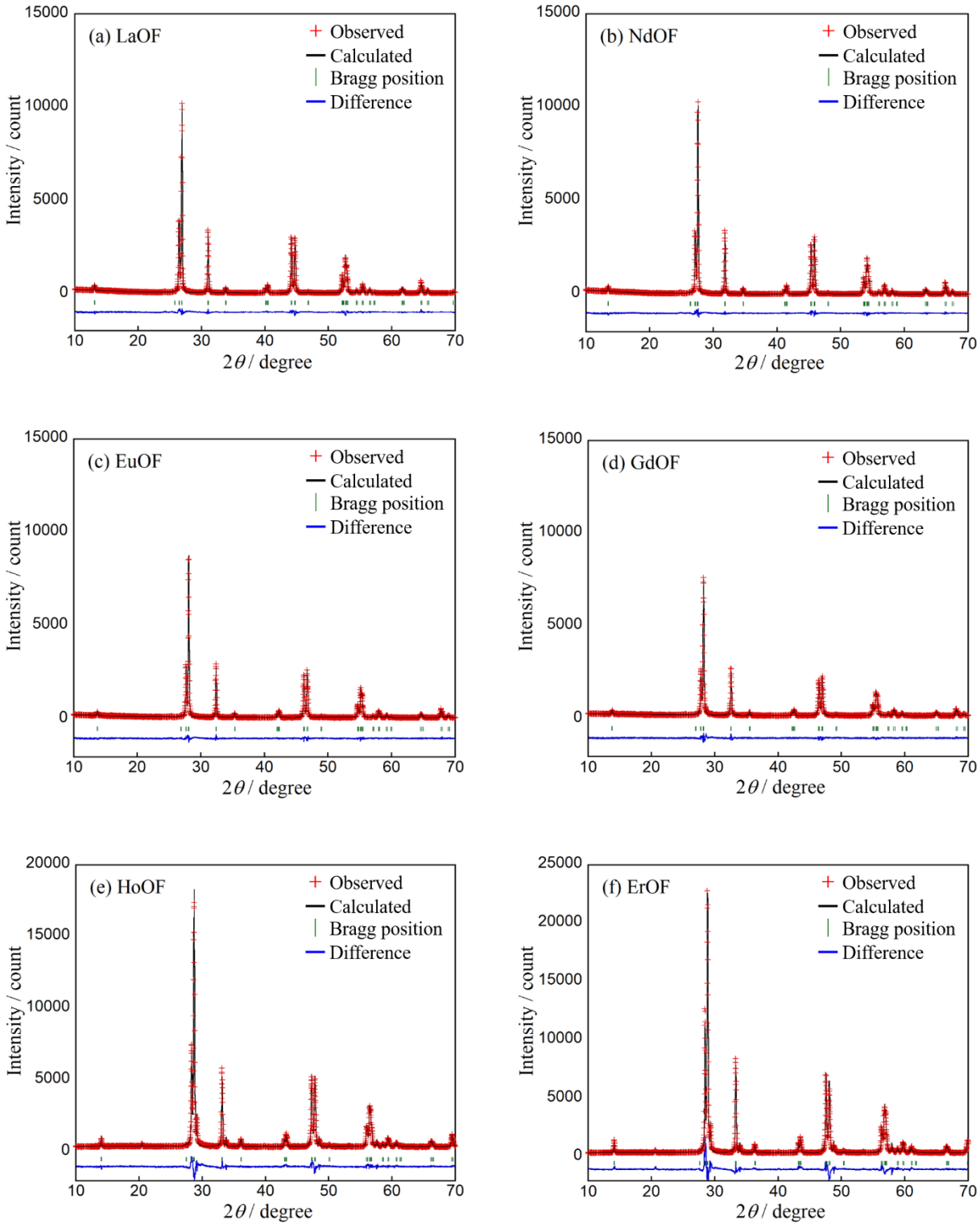


Figure 3.3 Rietveld refinement results for the (a) LaOF, (b) NdOF, (c) EuOF, (d) GdOF, (e) HoOF, and (f) ErOF solids.

Table 3.1 Structural parameters determined by the Rietveld refinement for the XRD (Cu-Kα) pattern of the *R*OF (y = 0.0) solids at room temperature

sample	atom	Wyckoff position	g	x	y	z	B / Å^2
LaOF	La	6c	1.0	0	0	0.2422(1)	0.1
	O	6c	1.0	0	0	0.1177(4)	0.7
	F	6c	1.0	0	0	0.3709(3)	0.7
Trigonal ($R\bar{3}m$, No. 166), a = 0.4051(1) nm, c = 2.0206(4) nm, α = β = 90°, γ = 120°, Z = 6, R_{wp} = 10.9 %, S = 1.42							
NdOF	Nd	6c	1.0	0	0	0.2420(4)	0.1
	O	6c	1.0	0	0	0.1206(4)	0.7
	F	6c	1.0	0	0	0.3696(3)	0.7
Trigonal ($R\bar{3}m$, No. 166), a = 0.3955(1) nm, c = 1.9699(3) nm, α = β = 90°, γ = 120°, Z = 6, R_{wp} = 11.2 %, S = 1.42							
EuOF	Eu	6c	1.0	0	0	0.7419(1)	0.1
	O	6c	1.0	0	0	0.6200(4)	0.7
	F	6c	1.0	0	0	0.8693(4)	0.7
Trigonal ($R\bar{3}m$, No. 166), a = 0.3886(1) nm, c = 1.9348(3) nm, α = β = 90°, γ = 120°, Z = 6, R_{wp} = 8.01 %, S = 1.21							
GdOF	Gd	6c	1.0	0	0	0.7418(6)	0.1
	O	6c	1.0	0	0	0.6198(4)	0.7
	F	6c	1.0	0	0	0.8691(4)	0.7
Trigonal ($R\bar{3}m$, No. 166), a = 0.3866(1) nm, c = 1.9254(4) nm, α = β = 90°, γ = 120°, Z = 6, R_{wp} = 6.67 %, S = 1.19							
HoOF	Ho	6c	1.0	0	0	0.7418(2)	0.1
	O	6c	1.0	0	0	0.6208(1)	0.7
	F	6c	1.0	0	0	0.8688(2)	0.7
Trigonal ($R\bar{3}m$, No. 166), a = 0.3804(1) nm, c = 1.8919(4) nm, α = β = 90°, γ = 120°, Z = 6, R_{wp} = 7.70 %, S = 1.93							
ErOF	Er	6c	1.0	0	0	0.7419(3)	0.1
	O	6c	1.0	0	0	0.6051(2)	0.7
	F	6c	1.0	0	0	0.8831(2)	0.7
Trigonal ($R\bar{3}m$, No. 166), a = 0.3789(1) nm, c = 1.8844(6) nm, α = β = 90°, γ = 120°, Z = 6, R_{wp} = 10.7 %, S = 2.90							

Table 3.2 Distances between *R*, O, and F atoms of the RO_4F_4 unit in the *R*OF (*R* = La, Nd, Eu, Gd, Ho, Er) solids

	LaOF	NdOF	EuOF	GdOF	HoOF	ErOF
$d_{R\text{-F1}}$ / nm	0.2604(7)	0.2515(7)	0.2465(7)	0.2451(9)	0.2401(5)	0.2382(6)
$d_{R\text{-F2}}$ / nm	0.2577(3)	0.2528(3)	0.2487(3)	0.2477(4)	0.2438(5)	0.2429(5)
$d_{R\text{-F1}}/d_{R\text{-F2}}$	1.0104	0.9948	0.9911	0.9895	0.9848	0.9805
$d_{R\text{-O1}}$ / nm	0.2476(8)	0.2399(9)	0.2359(8)	0.2349(9)	0.2290(5)	0.2303(6)
$d_{R\text{-O2}}$ / nm	0.2408(2)	0.2353(2)	0.2311(2)	0.2299(3)	0.2265(7)	0.2246(8)
$d_{R\text{-O1}}/d_{R\text{-O2}}$	1.0278	1.0195	1.0209	1.0217	1.0111	1.0253
$d_{F2\text{-F2}}$ / nm	0.4051(1)	0.3955(1)	0.3886(2)	0.3866(1)	0.3804(2)	0.3784(1)
$d_{O2\text{-O2}}$ / nm	0.4051(1)	0.3955(1)	0.3886(2)	0.3866(1)	0.3804(2)	0.3784(1)

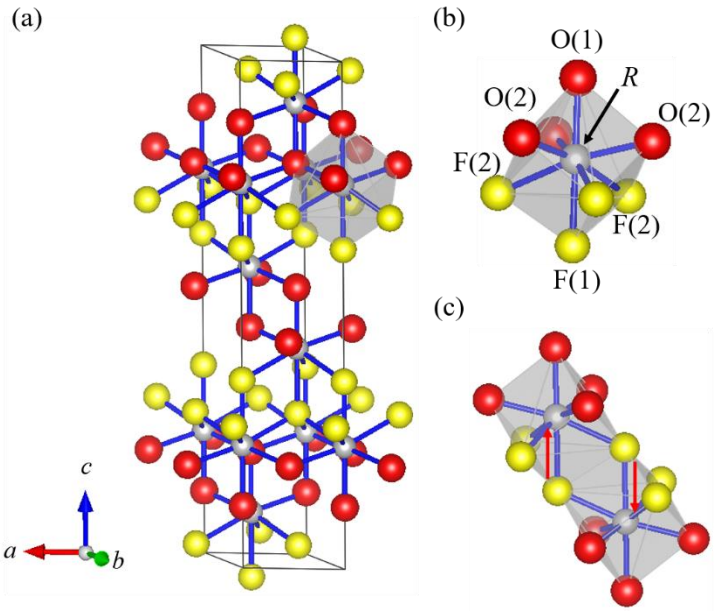


Figure 3.4 (a) Unit cell of trigonal *R*OF structure and (b) the RO_4F_4 local unit as expected from the Rietveld refinement. (c) Positional relationship between RO_4F_4 local units are also depicted.

To reveal the mechanism of the structural change from the trigonal ($R\bar{3}m$) phase to the tetragonal ($P4/nmm$) for *R* = La, Pr, orthorhombic ($Pmmn$) for *R* = Nd, Sm, Eu, and orthorhombic ($Abm2$) phases, which is caused by the introduction of F^- ions into *R*OF, the configuration of F and O around *R* in each

crystalline phase was compared (Figure 3.5). In the case of the tetragonal *P*4/*nmm* phase which is observed for the $RO_{1-y}F_{1+2y}$ (R = La, Pr; $0.1 \leq y \leq 0.4$) solids, the RO_4F_4 unit forms a tetragonal shape as in the $R\bar{3}m$ phase, while its arrangement of F and O is slightly different. Since the *R*–F and *R*–O distances are similar and the RO_4F_4 unit in the *R*OF ($y = 0.0$) solid is close to rectangular, the tetragonal shape of the RO_4F_4 unit can be maintained even when the O site in the $RO_{1-y}F_{1+2y}$ (R = La, Pr; $0.1 \leq y \leq 0.4$) solids is replaced by F atoms. In contrast, $RO_{1-y}F_{1+2y}$ (R = Nd–Yb) cannot be formed a tetragonal *P*4/*nmm* due to the large distortion of RO_4F_4 units, and lower symmetry *Pmmn* (Nd, Sm, Eu) and *Abm*2 (Gd–Yb) phases are formed depending on the degree of distortion of the RO_4F_4 units.

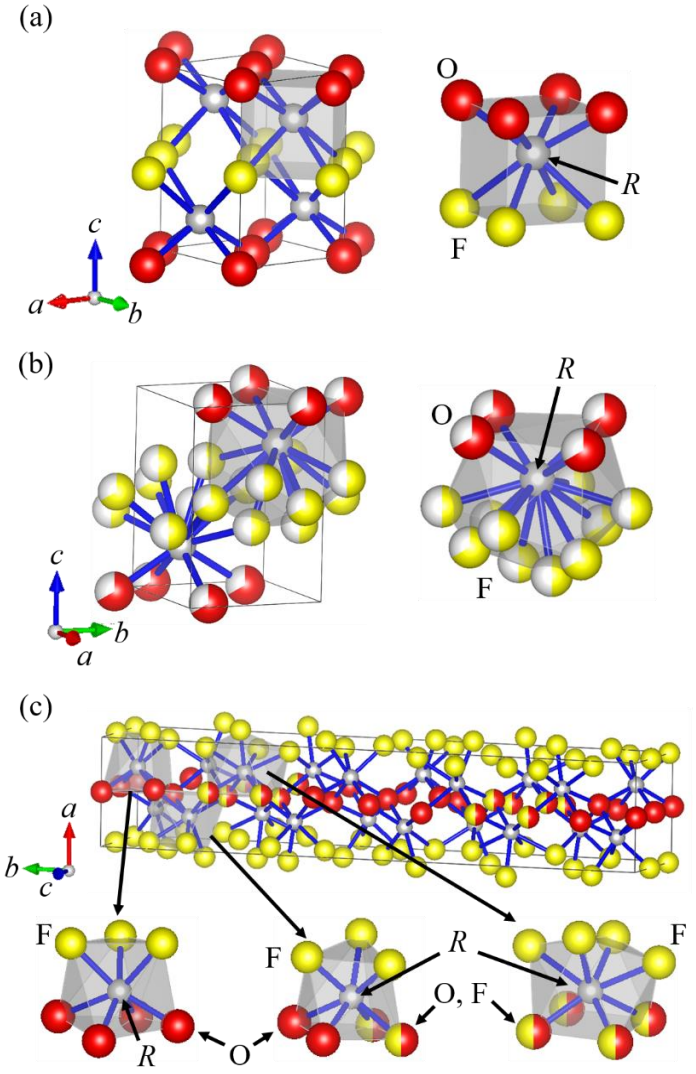


Figure 3.5 Schematic drawing of the crystal structure and the local structure around *R* in the rare earth oxyfluorides *R*OFs having (a) tetragonal (*P*4/*nmm*), (b) orthorohmic (*Pmmn*), and (c) orthorohmbic (*Abm*2) symmetry.

Figure 3.6 presents the composition dependencies of the ac conductivity at 300°C and the activation energies of these samples for the single-phase $RO_{1-y}F_{1+2y}$ ($0 \le y \le 0.4$; R = La, Pr, Nd, Sm, Eu, Gd, Tb, Dy, Ho, Er, Tm, Yb) solids. Activation energy was estimated from the conductivity values in the temperature between 300 to 500°C. In the single-phase samples with trigonal ($R\bar{3}m$) ROF structure, both an increase in conductivity and a decrease in activation energy were observed as decreasing the ionic radius of R^{3+} in the $RO_{1-y}F_{1+2y}$ solids, except for the LaOF and PrOF samples having higher symmetric RO_4F_4 unit in the structure. This tendency is due to shorter distance between F^- ions in the $RO_{1-y}F_{1+2y}$ structure. On the other hand, the conductivities of the LaOF and PrOF were higher than that of NdOF because of the lattice expansion which causes acceleration of ion migration. For the nonstoichiometric $RO_{1-y}F_{1+2y}$ ($0.1 \le y \le 0.4$) solids, there is a general trend that the conductivity

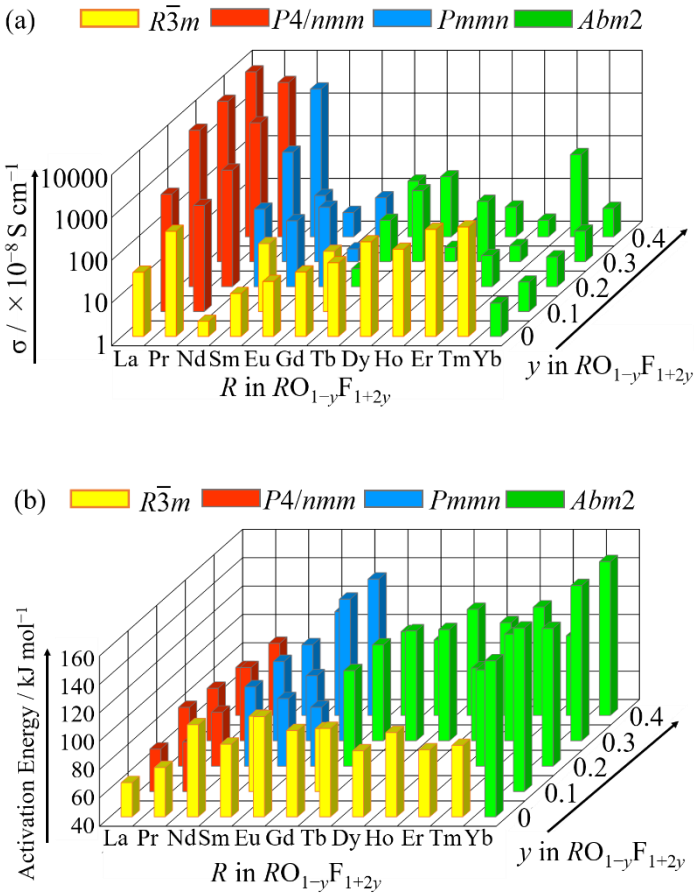


Figure 3.6 Compositional dependencies of (a) ac conductivity at 300°C and (b) activation energy for the single-phase of $RO_{1-y}F_{1+2y}$ (R = La, Pr, Nd, Sm-Yb; $0 \le y \le 0.4$) solids.

and activation energy decreased and increased, respectively, with lowering the symmetry of crystalline phase in the order of *P*4/*nmm*, *Pmmn*, and *Abm*2 phases. From this result, it is found that the structural distortion prohibits smooth ion migration. In addition, an increased tendency in conductivity was also observed with increasing *y*, which may be attributed to an increase in the number of conducting species in the structure.

3.4 Conclusions

Systematic studies of stoichiometric *R*OF (*R* = La, Pr, Nd, Sm, Eu, Gd, Tb, Dy, Ho, Er, Tm, Yb) solids showed that all *R*OF solids except YbOF formed a trigonal crystal structure. It was also revealed that the RO_4F_4 unit in the structure was distorted with a decrease of ionic radius of R^{3+} ion. Such local distortion occurred in the *R*OF structure resulted in the formation of different crystalline phases for the nonstoichiometric $RO_{1-y}F_{1+2y}$ solids. Among the crystal structures formed for the nonstoichiometric $RO_{1-y}F_{1+2y}$ solids, the solids with the tetragonal *P*4/*nmm* phase with the highest crystallographic symmetry exhibited the highest conductivity, due to the formation of ordered ion conducting pathway in the structure.

Summary

In the study of this thesis, the structural and F^- ion conducting properties in the rare-earth oxyfluorides (*R*OFs) which have the chemical and thermal stability was systematically investigated for developing the novel F^- ion conducting solid electrolytes applicable to the electrochemical devices like all-solid-state fluoride ion batteries (FIBs). For the deep understanding of *R*OFs, I synthesized nonstoichiometric solids varying F/O ratio together with stoichiometric *R*OF.

The results and findings obtained through this study are summarized as follows:

Chapter 1

To improve the fluoride ion conductivity and suppress the phase transition of the LaOF solid, the $La_{1-x}Mg_xO_{1-\delta}F$ solids with forming O^{2-} ion defects by partial replacement of Mg^{2+} ion into the La^{3+} ion site was prepared. The tetragonal structure (*P*4/*nmm*) was successfully stabilized for the sample with $x \geq 0.15$. Among the obtained samples, $La_{0.8}Mg_{0.2}O_{1-\delta}F$ ($x = 0.2$) solid showed the highest F^- ion conductivity of 6.9×10^{-3} S·cm^{-1} which is ca. 46.5 times higher than that of the stoichiometric LaOF ($x = 0$) solid at 800°C. The results obtained in this chapter indicate that the lattice contraction and the introduction of O^{2-} ion defects contribute to the suppression of phase transition and enhancement of the F^- ion conductivity.

Chapter 2

For the increase of F^- ion content in the LaOF, the $La_{1-x}Sr_xO_{0.6-0.5x-y}F_{1.8+2y}$ ($0 \leq x \leq 0.4$, $0 \leq y \leq 0.2$) solids were developed by doping larger Sr^{2+} ion (0.140 nm (CN = 8) [29]) than La^{3+} ion (0.130 nm (CN = 8) [29]) to expand the lattice and to generate O^{2-} ion defects. The $La_{0.7}Sr_{0.3}O_{0.4}F_{1.9}$ ($x = 0.3$, $y = 0.05$) solid exhibited approximately 30-fold and 4-fold higher F^- ion conductivity than the $La_{0.8}Mg_{0.2}O_{1-\delta}F$ and $LaO_{0.6}F_{1.8}$ solids, respectively. This result proves that F^- ion conducting properties of the LaOF solid can be accelerated even by introducing excess F^- ions into the lattice.

Chapter 3

The relationship between ionic conductivity and crystal phase for the *R*OF solids other than LaOF was systematically investigated by synthesizing nonstoichiometric rare-earth oxyfluorides, $RO_{1-y}F_{1+2y}$ ($0 \leq y \leq 0.4$; *R* = La, Pr, Nd, Sm, Eu, Gd, Tb, Dy, Ho, Er, Tm, and Yb), which varying F/O ratio. For the stoichiometric *R*OF ($y = 0$) except YbOF, all *R*OFs formed a trigonal structure ($R\bar{3}m$), with the RO_4F_4 unit gradually distorted as the ionic radius of R^{3+} decreased. Moreover, the conductivity of the *R*OF solids with trigonal structure except for *R* = La, Pr increased with decreasing the R^{3+} ionic radius for the trigonal *R*OF. In the case of nonstoichiometric $RO_{1-y}F_{1+2y}$ ($0.1 \leq y \leq 0.4$) solids with excess F^- ions introduced into the structure, a variety of structures were obtained depending on the rare-earth species; tetragonal ($P4/nmm$) for *R* = La, Pr, orthorhombic ($Pmmn$) for *R* = Nd, Sm, Eu, and orthorhombic ($Abm2$) phases for *R* = Gd, Tb, Dy, Ho, Er, Tm, Yb, respectively. The $LaO_{1-y}F_{1+2y}$ solid which has the most symmetric RO_4F_4 units in the structure exhibited the highest ion conductivity, and it was revealed that the structural symmetry of the $RO_{1-y}F_{1+2y}$ solids affects strongly to their ionic conductivity.

Refferences

[1] J. B. Goodenough and P. Singh, *J. Electrochem. Soc.*, **162**, (14), A2387–A2392 (2015).

[2] J. G. Kim, B. Son, S. Mukherjee, N. Schuppert, A. Bates, O. Kwon, M. J. Choi, H. Y. Chung, and S. Park, *J. Power Sources*, **282**, 299–322 (2015).

[3] S. C. Singhal, *Solid State Ionics*, **135**, 305–313 (2000).

[4] W. Jamsak, S. Assabmrungrat, P. L. Douglas, N. Laosiripojana, R. Suwanwarangkul, S. Charojrochkul, and E. Croiset, *Chem. Eng. J.*, **133**, 187–194 (2007).

[5] W. Weppner, *Mater. Sci. Eng.*, **B15**, 48–55 (1992).

[6] W. J. Fleming, *J. Electrochem. Soc.*, **124**, 21–28 (1977).

[7] N. Kayama, K. Homma, Y. Yamakawa, M. Hirayama, R. Kanno, M. Yonemura, T. Kamiyama, Y. Kato, S. Hama, K. Kawamoto, and A. Mitsui, *Nat. Mater.*, **10**, 682–686 (2011).

[8] L. J. Small, J. S. Wheeler, J. F. Ihlefeld, P. G. Clem, and E. D. Spoerke, *J. Mater. Chem. A*, **6**, 9691–9698 (2018).

[9] K. D. Kreuer, *Annu. Rev. Mater. Res.*, **33**, 333–359 (2003).

[10] G. C. Farrington and B. Dunn, *Solid State Ionics*, **7**, 267–281 (1982).

[11] K. Nomura, S. Ikeda, K. Ito, and H. Einaga, *Bull. Chem. Soc. Jpn.*, **65**, 3221–3227 (1992).

[12] M. Bralić, N. Radić, S. Brinić, and E. Generalić, *Talanta*, **55**, 581–586 (2001).

[13] M. Anji Reddy and M. Fichtner, *J. Mater. Chem.*, **21**, 17059–17062 (2011).

[14] M. D. Slater, D. Kim, E. Lee, and C. S. Johnson, *Adv. Funct. Mater.*, **23**, 947–958 (2013).

[15] F. Gschwind, G. Rodriguez-Garcia, D. J. S. Sandbeck, A. Gross, M. Weil, M. Fichtner, and N. Hörmann, *J. Fluorine Chem.*, **182**, 76–90 (2016).

[16] B. Dieudonnè, J. Chable, F. Mauvy, S. Fourcade, E. Durand, E. Lebraud, M. Leblanc, C. Legein, M. Body, V. Maisonneuve, and A. Demourgues, *J. Phys. Chem. C*, **119**, 25170–25179 (2015).

[17] V. Ya. Kavun, N. F. Uvarov, I. A. Telin, M. M. Polyantsev, A. B. Slobobyuk, O. V. Brovkina, and

B. K. Goncharuk, *Russ. J. Electrochem*., **41**, 560–572 (2005).

[18] M. Heise, G. Scholz, A. Düvel, P. Heitjans, and E. Kemnitz, *Solid State Ionics*, **60**, 65–74 (2016).

[19] K. Mori, A. Mineshige, T. Saito, M. Sugiura, T. Ishikawa, F. Fujisaki, K. Namba, T. Kamiyama, T. Otomo, T. Abe, and T. Fukunaga, *ACS Appl. Energy Mater.*, **3**, 2873–2880 (2020).

[20] J. Chable, B. Dieudonné, M. Body, C. Legein, M.-P. Crosnier-Lopez, C. Galven, F. Mauvy, E. Durand, S. Fourcade, D. Sheptyakov, M. Leblanc, V. Maisonneuve, and A. Demourgues, *Dalton Trans.*, **44**, 19625–19635 (2015).

[21] B. P. Sobolev, N. I. Sorokin, E. A. Krivandina, and Z. I. Zhmurova, *Crystallogr. Rep.*, **59**, 550-562 (2014).

[22] T. Petzel, V. Marx, and B. Hormann, *J. Alloys Compd.*, **200**, 27–31 (1993).

[23] J. P. Laval, A. Taoudi, and A. Abaouz, *J. Solid State Chem.*, **157**, 134–143 (2001).

[24] T, Wen, X. Li, D. Ning, J. Yao, B. Yang, and Y. Wang, *J. Mater. Chem. C*, **6**, 11007–11014 (2018).

[25] K. Niihara and S. Yajima, *Bull. Chem. Soc. Jpn.*, **44**, 643–648 (1971).

[26] K. T. Jacob, V. S. Saji, and Y. Waseda, *Int. J. Appl. Ceram. Tec.*, **3**, 312–321 (2006).

[27] J. W. Fergus and H. P. Chen, *J. Electrochem. Soc.*, **147**, 4696–4704 (2000).

[28] T. Wen, X. Li, D. Ning, J. Yao, B. Yang, and Y. Wang, *J. Mater. Chem. C*, **6**, 11007-11014 (2018).

[29] R. D. Shannon, *Acta Crystallogr. A*, **32**, 751–767 (1976).

[30] F. Izumi and K. Momma, *Sol. St. Phen.*, **130**, 15–20 (2007).

[31] J. Dabachi, M. Body, J. Dittmer, F. Fayon, and C. Legein, *Dalton Tran.*, **44**, 20675–20684 (2015).

[32] L. Beaury, J. Derouet, J. Holsa, M. Lastusaari, and C. Rodriguez, *Solid State Sci.*, **4**, 1039–1043 (2002).

[33] J. Hoelsae, E. Sailynoja, P. Ylha, P. Porcher, P. Deren, and W. Strek, *J. Phys. Chem.*, **100**, 14736–14744 (1996).

[34] S. E. Dutton, D. Hirai, and R. J. Cava, *Mater. Res. Bull.*, **47**, 714–718 (2012).

List of Publications

1. Crystal Phase Control and Ionic Conductivity of Magnesium Ion-Doped Lanthanum Oxyfluoride

Mizuki Momai, Shinji Tamura, Shohei Saeki, and Nobuhito Imanaka

Journal of the Ceramic Society of Japan, **128**, 863–865 (2020).

2. Fluoride Ion Conducting Behavior in Nonstoichiometric Lanthanum Oxyfluoride

Mizuki Momai, Shinji Tamura, and Nobuhito Imanaka

Ceramics International, **49**, 1502–1506 (2023).

3. Crystal Structure and Fluoride Ion Conducting Behavior of Nonstoichiometric Rare-earth Oxyfluoride

Mizuki Momai, Shinji Tamura, and Nobuhito Imanaka

Journal of the Ceramic Society of Japan, **132**, 55–57 (2024).

Acknowledgments

The author would like to express his deepest gratitude to Professor Dr. Nobuhito Imanaka, Division of Applied Chemistry, Graduate School of Engineering, Osaka University, for his continuous guidance, valuable advice during the process of this work.

The author is deeply in debt to Dr. Shinji Tamura, Division of Applied Chemistry, Graduate School of Engineering, Osaka University, for his continuous guidance and discussions for conducting this work. The author is also appreciated to Dr. Naoyoshi Nunotani, Division of Applied Chemistry, Graduate School of Engineering, Osaka University, for devoted advice and constructive suggestions.

The author would like to extend his sincere appreciation to Professor Dr. Ken-ichi Nakayama and Professor Dr. Hidehiro Sakurai, Divisions of Applied Chemistry, Graduate School of Engineering, Osaka University, for their constructive and valuable comments during the revision of this thesis.

Special thanks should be given to author's seniors and co-workers, Dr. Wonrak Lee, Dr. Muhammad Radzi Iqbal Bin Misran, Mr. Shohei Saeki, Mr. Takuya Morioki, Mr. Kentaro Yamada, Mr. Koki Yoshikawa, Mr. Takato Ishimura, Mr. Wataru Ochi, Mr. Masaya Asahi, Mr. Takahiro Horibe, Mr. Tatsuki Utsunomiya, Mr. Shunsuke Kondo, Mr. Eiji Takano, Mr. Koshiro Tanaka, Dr. Hiroaki Shirai, Dr. Kenji Matsuo, Mr. Won Joon Lee, Mr. Dongrun Hu, and Ms. Yo shimura for their helpful assistance and support in the process of this work, and the other members of the research group under direction of Professor Dr. Nobuhito Imanaka, Osaka University.

The author would also like to be grateful to Professor Dr. Atsushi Mineshige, Department of Chemical Engineering and Materials Science, Graduate School of Engineering, University of Hyogo, for great guidance and helpful encouragement.

Finally, the author would like to extend his deep appreciation to his parents, Mr. Kyoichi Momai and Mrs. Kaori Momai, His younger brother, Mr. Daigo Momai, and all members of his family for their encouragement, continuous understanding, and perpetual support.